Image Segmentation by Image Foresting Transform with Non-smooth Connectivity Functions

Lucy A. Choque Mansilla
Department of Computer Science,
University of São Paulo (USP),
05508-090, São Paulo, SP, Brazil.
Email: lucyacm@vision.ime.usp.br

Abstract—**Image segmentation, such as to extract an object from a background, is very useful for medical and biological image analysis. In this work, we propose new methods for interactive segmentation of multidimensional images, based on the Image Foresting Transform (IFT), by exploiting for the first time non-smooth connectivity functions (NSCF) with a strong theoretical background. The new algorithms provide global optimum solutions according to an energy function of graph cut, subject to high-level boundary constraints (polarity and shape), or consist in a sequence of paths' optimization in residual graphs. Our experimental results indicate substantial improvements in accuracy in relation to other state-of-the-art methods, by allowing the customization of the segmentation to a given target object.**

Keywords—*graph cut; image foresting transform; oriented image foresting transform; non-smooth connectivity function; geodesic star convexity*

I. INTRODUCTION

Image segmentation is one of the most fundamental and challenging problems in image processing and computer vision [1]. In medical image analysis, accurate segmentation results commonly require the user intervention because of the presence of structures with ill-defined borders, intensity non-standardness among images, field inhomogeneity, noise, artifacts, partial volume effects, and their interplay [2], [3]. The high-level, application-domain-specific knowledge of the user is also often required in the digital matting of natural scenes, because of their heterogeneous nature [4], [5]. These problems motivated the development of several methods for semi-automatic segmentation [6], [7], [8], [9], [10], [11], [12], aiming to minimize the user involvement and time required without compromising accuracy and precision.

One important class of interactive image segmentation comprises seed-based methods, which have been developed based on different theories, supposedly not related, leading to different frameworks, such as *watershed from markers* [9], [13], [14], *random walks* [15], *fuzzy connectedness* [16], [11], *graph cuts* [7], [17], *distance cut* [4], *image foresting transform* (IFT) [18], and *grow cut* [19]. The study of the relations among different frameworks, including theoretical and empirical comparisons, has a vast literature [20], [21], [22], [23]. However, these methods in most studies are restricted to undirected graphs, and the most time-efficient methods, including the IFT, present a lack of boundary regularization constraints. Moreover, the quality of their segmentation results with minimal user intervention, strongly depends on an adequate estimate of the weights assigned to the graph's arcs [24].

The main contribution of this work is a theoretical development to support the usage of **non-smooth connectivity functions** (NSCF) in the IFT, opening new perspectives in the research of image processing using graphs, since NSCF were, until now, avoided in the literature. More specifically, we prove that some NSCF can lead to optimum results according to a graph-cut measure on a digraph [25], [26] or consist in a sequence of paths' optimization in residual graphs. We have as main results:

1) The customization of the segmentation by IFT to match the global and local features of a target object:

   (a) The design of more adaptive and flexible connectivity functions, which allow better handling of images with strong inhomogeneity by using dynamic weights.
   (b) The orientation of the object's intensity transitions, i.e., bright to dark or the opposite (boundary polarity).
   (c) The shape constraints to regularize the segmentation boundary (geodesic star convexity constraint).

2) The development of an interactive segmentation tool within the software, called *Brain Image Analyzer* (BIA), to support research in neurology involving volumetric magnetic resonance images of a 3T scanner from the FAPESP-CInApCe (Figure 1).

3) A total of four conference papers were published in international events of high regard [26], [27], [28], [29], and one journal paper was published in the *IEEE Transactions on Image Processing* (impact factor: 3.111) [25].

For the sake of completeness in presentation, Section II includes the relevant previous work of image segmentation by IFT. In Sections III, IV, V and VI, we present the main contributions covered in the master's dissertation [30]: The classification of NSCF, the use of adaptive weights via NSCF, the boundary polarity through digraphs, and the elimination of false delineations by shape constraints. Our conclusions are stated in Section VII.
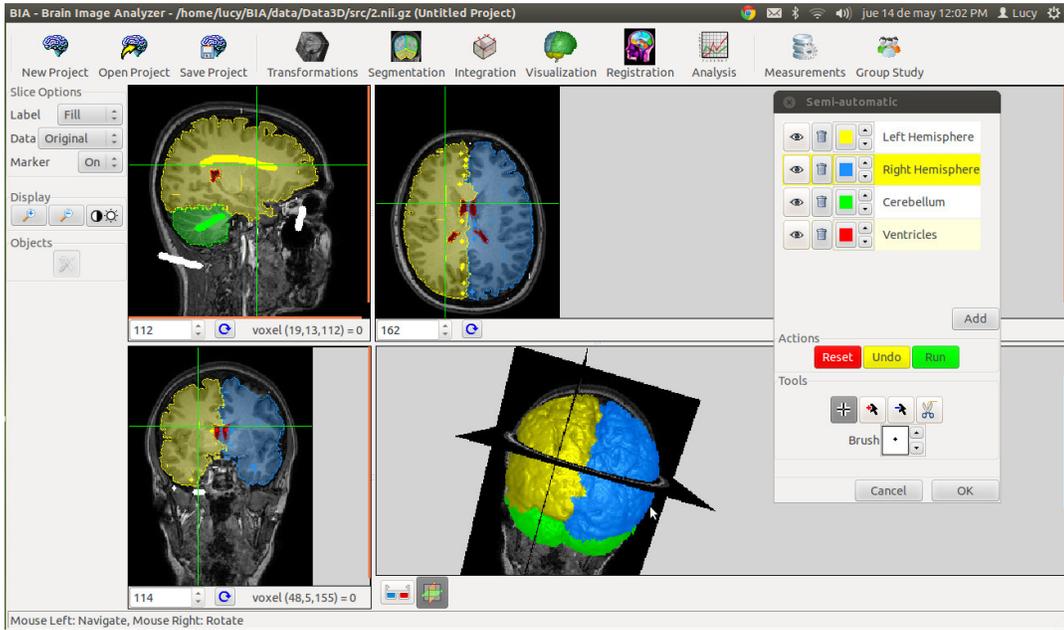
Fig. 1. Example of an interactive segmentation in progress of multiple objects in a 3D MRI image for user-selected markers using the software Brain Image Analyzer (BIA).

II. IMAGE FORESTING TRANSFORM (IFT)

An image 2D/3D can be interpreted as a weighted digraph $G = \langle \mathcal{V} = \mathcal{I}, \xi, \omega \rangle$ whose nodes $\mathcal{V}$ are the image pixels in its image domain $\mathcal{I} \subset \mathbb{Z}^N$, and whose arcs are the ordered pixel pairs $(s, t) \in \xi$ (e.g., 4-neighborhood, or 8-neighborhood, in case of 2D images, and 6-neighbors in 3D). The digraph G is symmetric if for any of its arcs (s, t), the pair (t, s) is also an arc of G. We have an undirected graph when $\omega(s, t) = \omega(t, s)$ in a symmetric graph G. We use $(s, t) \in \xi$ or $t \in \xi(s)$ to indicate that t is adjacent to s. Each arc $(s, t) \in \xi$ may have a weight $\omega(s, t) \geq 0$, such as a dissimilarity measure between pixels s and t (e.g., $\omega(s, t) = |I(t) - I(s)|$ for a single channel image with values given by $I(t)$).

For a given image graph G, a path $\pi_t = \langle t_1, t_2, \ldots, t_n = t \rangle$ is a sequence of adjacent pixels with terminus at a pixel t. A path is *trivial* when $\pi_t = \langle t \rangle$. A path $\pi_t = \pi_s \cdot \langle s, t \rangle$ indicates the extension of a path π_s by an arc (s, t). The notation $\pi_{s \rightsquigarrow t} = \langle t_1 = s, t_2, \ldots, t_n = t \rangle$ may also be used, where s stands for the origin and t for the destination node.

A *predecessor map* is a function P that assigns to each pixel t in $\mathcal{V}$ either some other adjacent pixel in $\mathcal{V}$, or a distinctive marker nil not in $\mathcal{V}$ — in which case t is said to be a *root* of the map. A *spanning forest* is a predecessor map which contains no cycles — i.e., one which takes every pixel to nil in a finite number of iterations. For any pixel $t \in \mathcal{V}$, a spanning forest P defines a path π_t^P recursively as $\langle t \rangle$ if $P(t) = nil$, and $\pi_s^P \cdot \langle s, t \rangle$ if $P(t) = s \neq nil$.

A *connectivity function* computes a value $f(\pi_t)$ for any path π_t, usually based on arc weights. A path π_t is *optimum* if $f(\pi_t) \leq f(\tau_t)$ for any other path τ_t in G. By taking to each pixel $t \in \mathcal{V}$ one optimum path with terminus t, we obtain the optimum-path value $V(t)$, which is uniquely defined by $V(t) = \min_{\forall \pi_t \text{ in } G} \{ f(\pi_t) \}$. A path $\pi_{t_n} = \langle t_1, t_2, \ldots, t_n \rangle$ is *complete optimum* if all paths $\pi_{t_i} = \langle t_1, t_2, \ldots, t_i \rangle$, $i = 1, 2, \ldots, n$ are optimum paths.

The IFT takes an image graph G, and a path-cost function f; and assigns one optimum path π_t to every pixel $t \in \mathcal{V}$ such that an *optimum-path forest* P is obtained — i.e., a spanning forest P where all paths π_t^P, $t \in \mathcal{V}$, are optimum. However, f must be *smooth* (Definition 1), otherwise, the paths may not be optimum [18].

Definition 1 (Smooth path-cost function). *A path-cost function f is* smooth *if for any pixel $t \in \mathcal{I}$, there is an optimum path π_t, which either is trivial, or has the form $\pi_s \cdot \langle s, t \rangle$ where*

(C1) $f(\pi_s) \leq f(\pi_t)$,
(C2) π_s *is optimum,*
(C3)   *C2 is valid and for any optimum path π_s' ending at s, $f(\pi_s' \cdot \langle s, t \rangle) = f(\pi_t)$.*

The cost of a trivial path $\pi_t = \langle t \rangle$ is usually given by a handicap value $H(t)$, while the connectivity functions for non-trivial paths follow a path-extension rule. For example:

$$f_{\max}(\pi_t = \pi_s \cdot \langle s, t \rangle) = \max \{ f_{\max}(\pi_s), \omega(s, t) \} \quad (1)$$

$$f_{sum}(\pi_t = \pi_s \cdot \langle s, t \rangle) = f_{sum}(\pi_s) + \omega_2(s, t) \quad (2)$$

$$f_{\omega}(\pi_t = \pi_s \cdot \langle s, t \rangle) = \omega(s, t) \quad (3)$$

where $\omega(s, t) \geq 0$ and $\omega_2(s, t) \geq 0$ are fixed arc weights.

We consider image segmentation from two seed sets, $\mathcal{S}_o$ and $\mathcal{S}_b$ ($\mathcal{S}_o \cap \mathcal{S}_b = \emptyset$), containing pixels selected inside and outside the object, respectively. The search for optimum paths is constrained to start in $\mathcal{S} = \mathcal{S}_o \cup \mathcal{S}_b$ (i.e., $H(t) = 0$ for all $t \in \mathcal{S}$, and $H(t) = +\infty$ otherwise). The image is partitioned into two optimum-path forests — one rooted at the internal

seeds, defining the object, and the other rooted at the external seeds, representing the background. A label, $L(t) = 1$ for all $t \in \mathcal{S_o}$ and $L(t) = 0$ for all $t \in \mathcal{S_b}$, is propagated to all unlabeled pixels during the computation [18].

In the IFT, the optimum-path forest may not be unique [18]. For example, if two or more seeds lead to a pixel t through optimum paths with the same cost , then more than one forest may be optimum. Paths $\pi_{r_1 \rightsquigarrow t}$ and $\tau_{r_2 \rightsquigarrow t}$ with the same label (i.e., $\{r_1, r_2\} \subset \mathcal{S_o}$ or $\{r_1, r_2\} \subset \mathcal{S_b}$) are not a problem, because they lead to the same segmentation result and any solution is satisfactory. For paths with different labels, we have the basis of the real *tie zones*. The *tie zones* are the maximal set of *tie-zone pixels* [1], which forms a subtree in some optimum-path forest [31].

III. IFT WITH NON-SMOOTH CONNECTIVITY FUNCTIONS

Clearly, from Definition 1, we have that a connectivity function is not smooth if it doesn't satisfy at least one of the conditions C1, C2 or C3. For example the functions $f_{\Sigma \max}$, $f_{\sum |\triangle I|}$, $f_{\max |\triangle I|}$, $f_{\updownarrow}$ and $f_{\max}^{bkg}$ [2] violate C2 and C3:

$$f_{\Sigma \max}(\pi_t = \langle t \rangle) = \begin{cases} 0, & \text{if } t \in \mathcal{S}, \\ +\infty, & \text{otherwise.} \end{cases}$$
$$f_{\Sigma \max}(\pi_t = \pi_s \cdot \langle s, t \rangle) = f_{\Sigma \max}(\pi_s) + f_{\max}(\pi_t) \quad (4)$$

$$f_{\sum |\triangle I|}(\pi_t = \langle t \rangle) = \begin{cases} 0, & \text{if } t \in \mathcal{S}, \\ +\infty, & \text{otherwise.} \end{cases}$$
$$f_{\sum |\triangle I|}(\pi_t = \pi_{r \rightsquigarrow s} \cdot \langle s, t \rangle) = f_{\sum |\triangle I|}(\pi_{r \rightsquigarrow s}) + |I(t) - I(r)| \quad (5)$$

$$f_{\max |\triangle I|}(\pi_t = \langle t \rangle) = \begin{cases} 0, & \text{if } t \in \mathcal{S}, \\ +\infty, & \text{otherwise.} \end{cases}$$
$$f_{\max |\triangle I|}(\pi_t = \pi_{r \rightsquigarrow s} \cdot \langle s, t \rangle) = \max \{ f_{\max |\triangle I|}(\pi_{r \rightsquigarrow s}), \\ |I(t) - I(r)| \} \quad (6)$$

$$f_{\updownarrow}(\pi_t = \langle t \rangle) = \begin{cases} 0, & \text{if } t \in \mathcal{S}, \\ +\infty, & \text{otherwise.} \end{cases}$$
$$f_{\updownarrow}(\pi_t = \pi_s \cdot \langle s, t \rangle) = f_{Imax}(\pi_t) - f_{Imin}(\pi_t) \quad (7)$$

where f_{Imax} and f_{Imin} are functions that take the maximum and minimum intensity values along the path, respectively:

$$f_{Imax}(\pi_t = \langle t \rangle) = I(t)$$
$$f_{Imax}(\pi_t = \pi_s \cdot \langle s, t \rangle) = \max \{ f_{Imax}(\pi_s), I(t) \} \quad (8)$$

and

$$f_{Imin}(\pi_t = \langle t \rangle) = I(t)$$
$$f_{Imin}(\pi_t = \pi_s \cdot \langle s, t \rangle) = \min \{ f_{Imin}(\pi_s), I(t) \} \quad (9)$$

---

[1] A pixel t is a *tie-zone pixel* if there exist two complete optimum paths $\pi_{r_1 \rightsquigarrow t}$ and $\tau_{r_2 \rightsquigarrow t}$ such that $r_1 \in \mathcal{S_b}$ and $r_2 \in \mathcal{S_o}$.

[2] The function $f_{\max}^{bkg}$ incorporates a tie-breaking rule inside its path-value definition to resolve ties of the function $f_{\max}$ (Equation 1) by favoring background seeds. Since this is the same behavior exhibited by the *Iterative Relative Fuzzy Connectedness* (IRFC), the formulation of $f_{\max}^{bkg}$ corresponds to an alternative IFT-based codification for the IRFC method [32].

where $I(t)$ is the intensity of a pixel t.

$$f_{\max}^{bkg}(\pi_t = \langle t \rangle) = \begin{cases} -1 & \text{if } t \in \mathcal{S_o} \cup \mathcal{S_b} \\ +\infty & \text{otherwise} \end{cases}$$
$$f_{\max}^{bkg}(\pi_t = \pi_{r \rightsquigarrow s} \cdot \langle s, t \rangle) = \begin{cases} Expr1 & \text{if } r \in \mathcal{S_o} \\ Expr2 & \text{if } r \in \mathcal{S_b} \end{cases} \quad (10)$$

$$Expr1 = \max \{ f_{\max}^{bkg}(\pi_{r \rightsquigarrow s}), 2 \times \omega(s, t) + 1 \}$$
$$Expr2 = \max \{ f_{\max}^{bkg}(\pi_{r \rightsquigarrow s}), 2 \times \omega(s, t) \}$$

In [29], we formally classified several non-smooth functions according to the conditions C1, C2 and C3 (Definition 1), and C4 (Definition 2).

Definition 2 (Condition C4). *A path-value function f satisfies the condition C4, if for any node $s \in \mathcal{I}$ the following condition is verified $\forall t \in \xi(s)$:*

- *For any paths π_s and π_s' ending at s, if $f(\pi_s) = f(\pi_s')$, then we have $f(\pi_s \cdot \langle s, t \rangle) = f(\pi_s' \cdot \langle s, t \rangle)$.*

For a general image graph, the classification of various non-smooth functions into the sets C_1, C_2, C_3, and C_4 (such that a function f is in a set C_i if and only if it satisfies the condition C_i) is shown in the proposed diagram illustrated in Figure 2. The functions $f_\omega^\circlearrowright$, $f_{i,\omega}$ and $f_{o,\omega}$ were studied in [33], [26], and f_I are defined in [29].
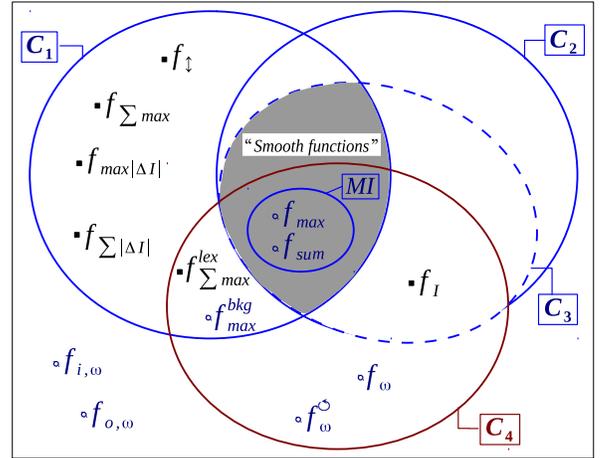
Fig. 2. Schematic representation of the relations between smooth and non-smooth connectivity functions: C_1, C_2, C_3 and C_4 are sets of connectivity functions that satisfy these respective conditions for a general graph.

Some functions in the subset $C_1 \setminus (C_2 \bigcup C_4)$ have corresponding variations in the region $(C_1 \cap C_4) \setminus C_2$ of the diagram. That is possible by using a second cost component with comparisons in lexicographic order. For example, the lexicographical function $f_{\Sigma \max}^{lex}$ (Equation 11) is a variation of the non-smooth function $f_{\Sigma \max}$ (Equation 4).

$$f_{\Sigma \max}^{lex}(\pi_t = \langle t \rangle) = \begin{cases} (0, 0), & \text{if } t \in \mathcal{S}, \\ (+\infty, +\infty), & \text{otherwise.} \end{cases}$$
$$f_{\Sigma \max}^{lex}(\pi_t = \pi_s \cdot \langle s, t \rangle) = (f_{\Sigma \max}(\pi_t), f_{\max}(\pi_t)). \quad (11)$$

IV. ADAPTIVE WEIGHTS VIA NSCF

Methods based on IFT [18] have been successfully used in the segmentation of 1.5 Tesla MR datasets [34], [35]. However, inhomogeneity effects are stronger in higher magnetic fields (Figure 3), and it is extremely important to define the optimal solution for these images. NSCFs are more adaptive to cope with the problems of field inhomogeneity, which are common in MR images of 3 Tesla [36].

(a)   (b)   (c)

(d)   (e)   (f)
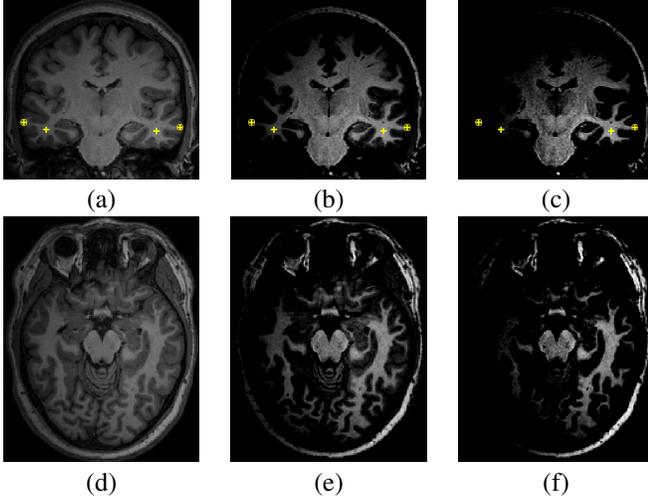
Fig. 3. Example of field inhomogeneity. (a) The yellow markers +/⊕ indicate corresponding regions in different tissues of the hemispheres. On the left, the gray and white matter show intensity values of 57 and 145, respectively, for the selected points. In the right region of the image, we have considerably higher values, 109 and 221. (a-c) By varying the brightness and contrast configurations, it is possible to better observe the problem. (d-f) Variations of brightness and contrast in an axial slice, revealing the inhomogeneity.

In order to give a theoretical foundation to support the usage of NSCF, we theoretically proved that the IFT with any non-smooth function $f \in (C_1 \cap C_4) \setminus C_2$ is, in fact, equivalent to the result of a sequence of optimizations, each of them involving a maximal set of elements, in a well-structured way [29]. This proof was supported by the following proposition:

Proposition 1. *Consider a function $f \in (C_1 \cap C_4) \setminus C_2$. For a given image graph $G = \langle \mathcal{V}, \xi, \omega \rangle$, and set of seeds $\mathcal{S}$, let O be the set of all pixels $t \in \mathcal{V}$, such that there exists a complete-optimum path π_t for f. In any spanning forest P computed in G by the IFT algorithm for f, all the paths τ_t^P with $t \in O$ are optimum paths.*

Consider the following definitions: Let $\xi^{set}(X) = \{(s,t) \in \xi \mid s \in X \wedge t \in X\}$ denote the set of all arcs interconnecting nodes in the set X, $\xi^{path}(\pi)$ denote the set of all arcs in the path π (i.e., $\xi^{path}(\pi) = \{(t_i, t_{i+1}) \text{ for } 1 \leq i \leq k-1 \mid \pi = \langle t_1, t_2, \ldots, t_i, t_{i+1}, \ldots, t_k \rangle\}$), $\xi^{cut}(X,Y) = \{(s,t) \in \xi \mid s \in X \wedge t \in Y\}$, $\xi^{pred}(X) = \bigcup_{\forall t \in X} \xi^{path}(\pi_t^P)$.

In the first optimization step, optimum paths τ_t^P are computed for all $t \in O$ (Proposition 1). Let's denote O as O^1 for this first step. In the next optimization step, consider the subgraph $G^2 = \langle \mathcal{I}, \xi^{set}(\mathcal{I} \setminus O^1) \cup \xi^{cut}(O^1, \mathcal{I} \setminus O^1) \cup$

$\xi^{pred}(O^1), \omega \rangle$. A second path optimization is performed, by computing a second IFT, but now in G^2 [3]. Since the arcs interconnecting nodes in O^1, are reduced to the arcs in the previous forest P (i.e., $\xi^{pred}(O^1)$) in G^2, we have that the optimum paths τ_t^P, computed on the previous step, will remain optimum in the new graph G^2. So the optimum paths τ_t^P with $t \in O^1$ will start a new competition, seeking for their best extensions to the other pixels in $\mathcal{I} \setminus O^1$. By applying the Proposition 1 on this new optimization problem one more time, we have that this second IFT will conquer a new maximal set of pixels $O^1 \cup O^2$ that can be reached by optimum paths in G^2. We can then repeat this process over again. The condition $C1$ [4] guarantees that at least one new element will be conquered at each step, so that this process will repeat until $\bigcup_{\forall i} O^i = \mathcal{I}$.

Figure 4 shows an example of the ordered process about the sequence of optimizations for a non-smooth function $f_{\Sigma \max}^{lex} \in (C_1 \cap C_4) \setminus C_2$.

Figure 5 shows an example about the benefits of the non-smooth function $f_{\max |\triangle I|}$ (Equation 6) compared to the smooth connectivity function $f_{\max}$ (Equation 1) in image segmentation with inhomogeneity problem. Note that the function $f_{\max |\triangle I|}$ is more adaptive to cope with problems of inhomogeneity, by offering adaptive weights to the pixels in the image graph.

In our experiments, we used 10 T1-weighted 3D images of male and female adults with normal brains. The image dataset included the head and, at least, a small portion of the neck. Our experimental result, using a robot user [5] for segmenting the brain dataset, indicates that substantial improvements can be obtained by NSCFs in the 3D segmentation of MR images of 3 Tesla, with strong inhomogeneity effects, when compared to smooth connectivity functions. That is because NSCFs permit a more adaptive configuration of the arc weights.

Figure 6 shows the experimental curves, where $IRFC$ [16] and $PW_{q=2}$ [23] represent different algorithms related to the smooth function $f_{\max}$, and we used $\omega(s,t) = G(s) + G(t)$, where $G(s)$ is the magnitude of Sobel gradient at a voxel s. Clearly, $f_{\Sigma |\triangle I|}^{lex}$ presented the best accuracy. Figures 7 and 8 show examples for user-selected markers. These results emphasize the importance of non-smooth connectivity functions. The non-smooth connectivity function $f_{\Sigma |\triangle I|}^{lex}$ is a variation of $f_{\Sigma |\triangle I|}$ (Equation 5), in order to guarantee that $f_{\Sigma |\triangle I|}^{lex} \in (C_1 \cap C_4) \setminus C_2$. The function $f_{\Sigma |\triangle I|}^{lex}$ gives pairs of values that should be compared according to the lexicographical order. The first component is the non-smooth function $f_{\Sigma |\triangle I|}$ (Equation 5), and the second is the priority level of the seed/root for that path. The lower its value the higher is its priority. In interactive segmentation, we give lower priority for new inserted seeds, since they are used mainly for corrective actions, so that we can keep their effects more locally. The same process was done for $f_{\max |\triangle I|}^{lex} \in (C_1 \cap C_4) \setminus C_2$ and $f_{\updownarrow}^{lex} \in (C_1 \cap C_4) \setminus C_2$, in relation to $f_{\max |\triangle I|}$ (Equation 6) and $f_{\updownarrow}$ (Equation 7), respectively [29].

---

[3] By IFT algorithm, the pixels $s \in O^1$ have a defined status, and their paths can't be changed. Therefore, we consider a new graph G^2, where the arcs interconnecting nodes in O^1 which are not in the forest P are disregarded.

[4] By the hypothesis, we know that f satisfies the condition $C1$.

[5] Method introduced in [37], to simulate user interaction of interactive segmentation.
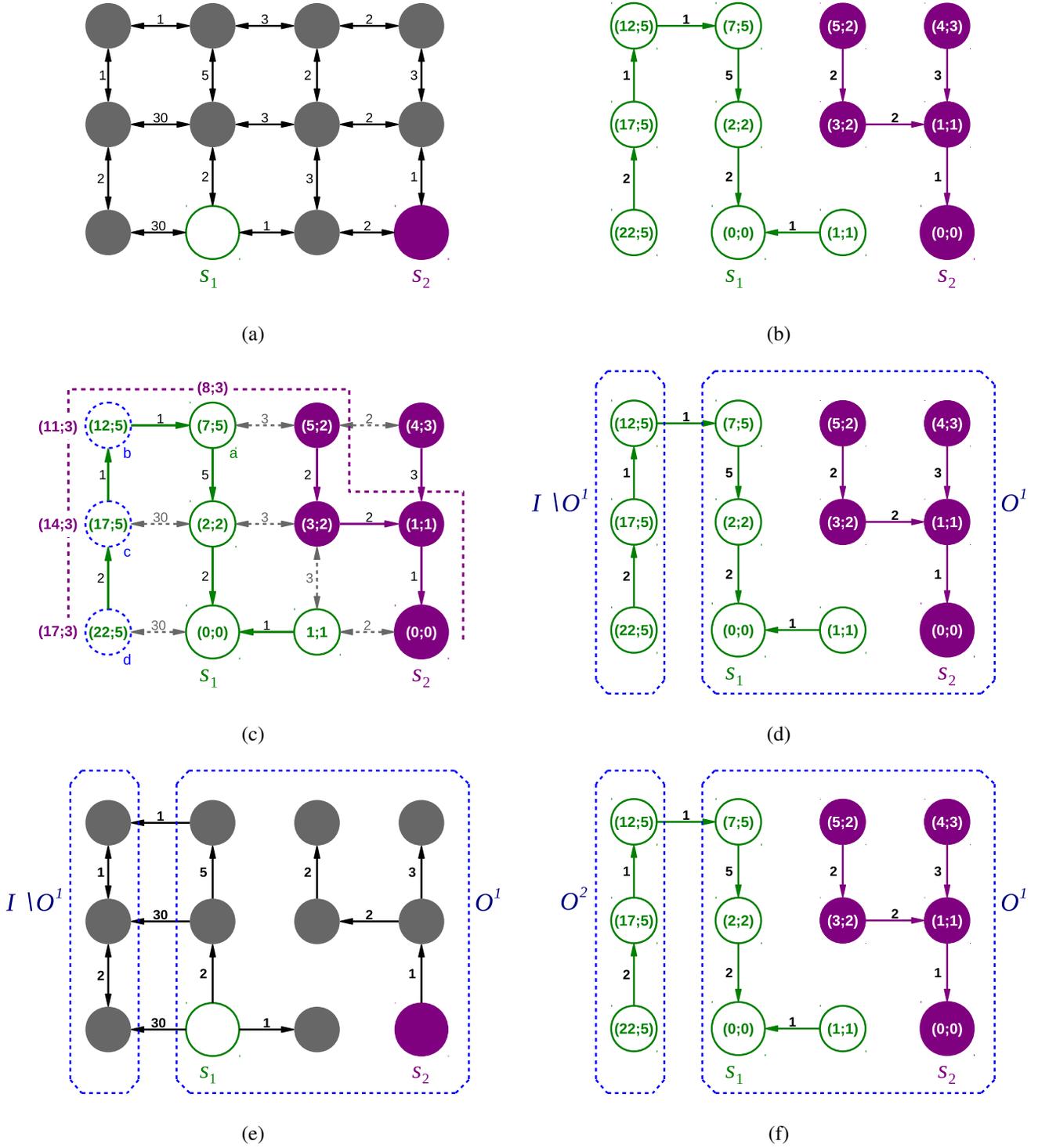
Fig. 4. (a) An image graph G using 4-neighbors for pixel adjacency and seeds $\boldsymbol{S} = \{s_1, s_2\}$, where the numbers in the arcs represent their weights. (b) Spanning forest computed by the IFT with a non-smooth function $f_{\Sigma \max}^{lex} \in (\boldsymbol{C_1} \bigcap \boldsymbol{C_4}) \backslash \boldsymbol{C_2}$. The numbers inside the nodes indicate values of the path-value map V with two components in lexicographical order. In this figure the arrows indicate the predecessor map. (c) Note that the path $\pi_{s_1 \rightsquigarrow a}$ is a complete-optimum path, but the path $\pi_{s_1 \rightsquigarrow b}$ is not optimum, since that there is another path $\pi'_{s_2 \rightsquigarrow b}$, following the dashed line, offering a better cost (i.e., $f_{\Sigma \max}^{lex}(\pi'_{s_2 \rightsquigarrow b}) = (11;3) < f_{\Sigma \max}^{lex}(\pi_{s_1 \rightsquigarrow b}) = (12;5)$). This shows that the function $f_{\Sigma \max}^{lex}$ is not smooth. (d) By applying the Proposition 1 we have a forest computed for the set $\boldsymbol{O^1}$, composed of optimum paths in the graph G (i.e., first optimization). (e) We have the residual graph G^2, which will be used in a second optimization. (f) Optimum forest computed from the graph G^2, ending the process with $\boldsymbol{O^1} \bigcup \boldsymbol{O^2} = \boldsymbol{\mathcal{I}}$.
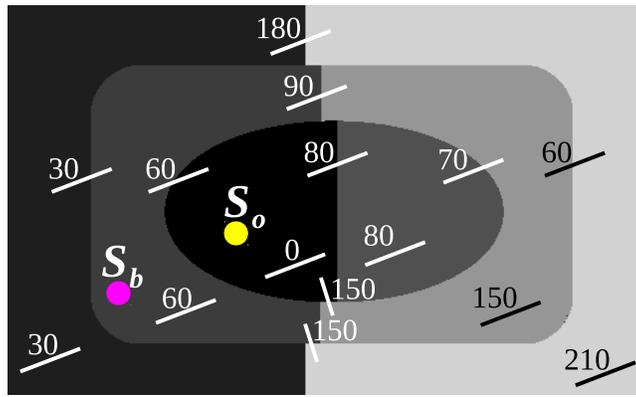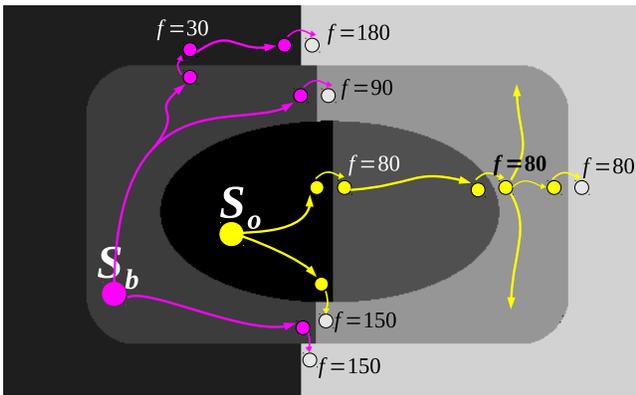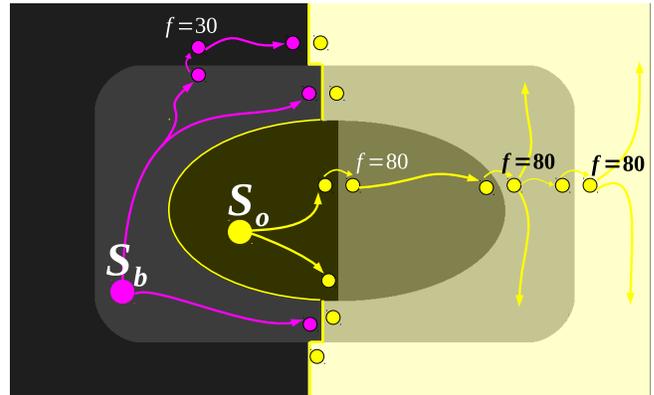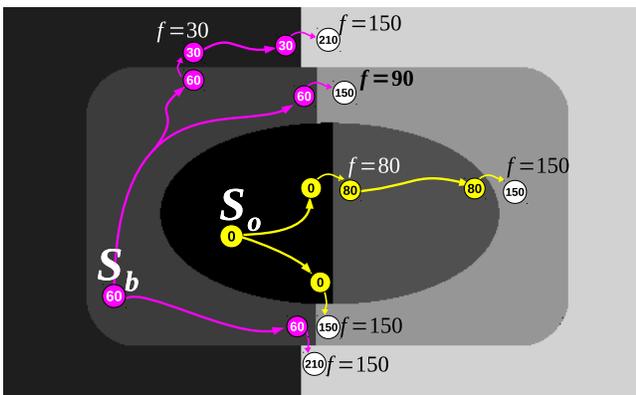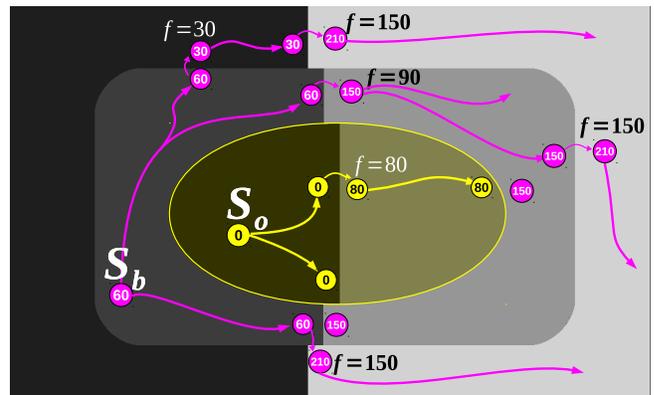
Fig. 5. (a) Synthetic image with problem of inhomogeneity. The target object for the image segmentation is the central object with elliptical shape. The user-selected markers are the seeds S_o and S_b. The numbers are some representative arc values $\omega(s,t)$ depicted for each region and border segment. (b-c) Schematic representation of the path costs f offered by the seeds for the pixels in the image using the smooth function f_{max} and the segmentation result. (d-e) Schematic representation of the path costs f offered by the seeds for the pixels in the image using the non-smooth function $f_{max\,|\triangle I|}$ and the segmentation result. The values inside of the nodes represent the intensities of the pixels.
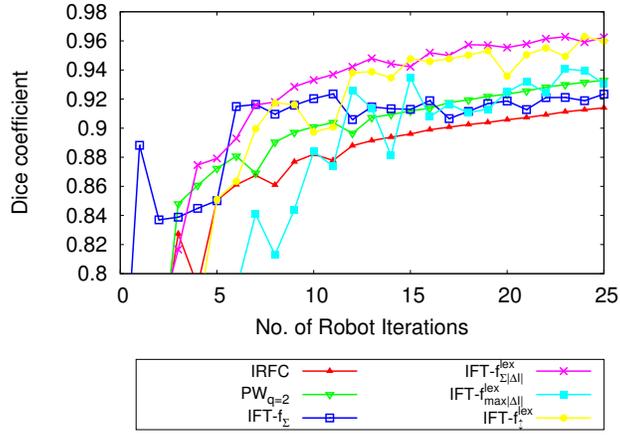
Fig. 6.   Results using a robot user for segmenting the 3D brain dataset.
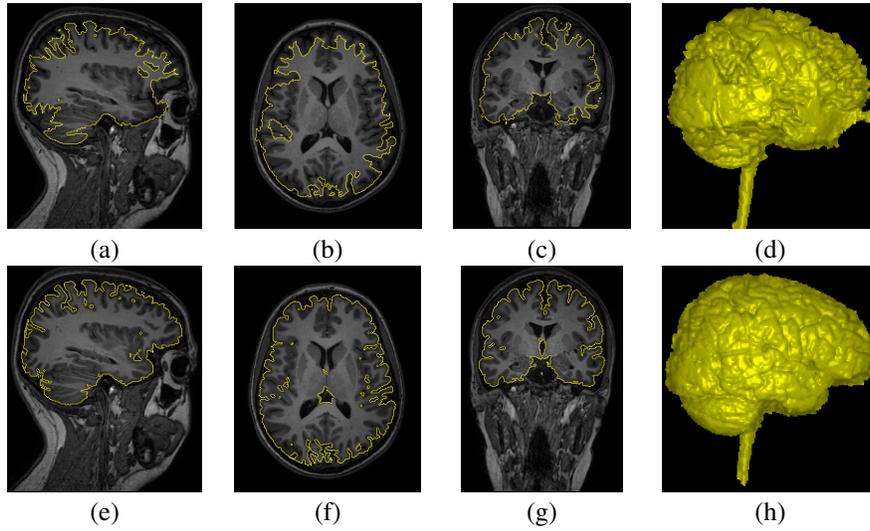
Fig. 7.   Brain segmentation results for the same user-selected markers by (a-d) $f_{\max}$, and (e-h) $f^{lex}_{\sum|\triangle I|}$.
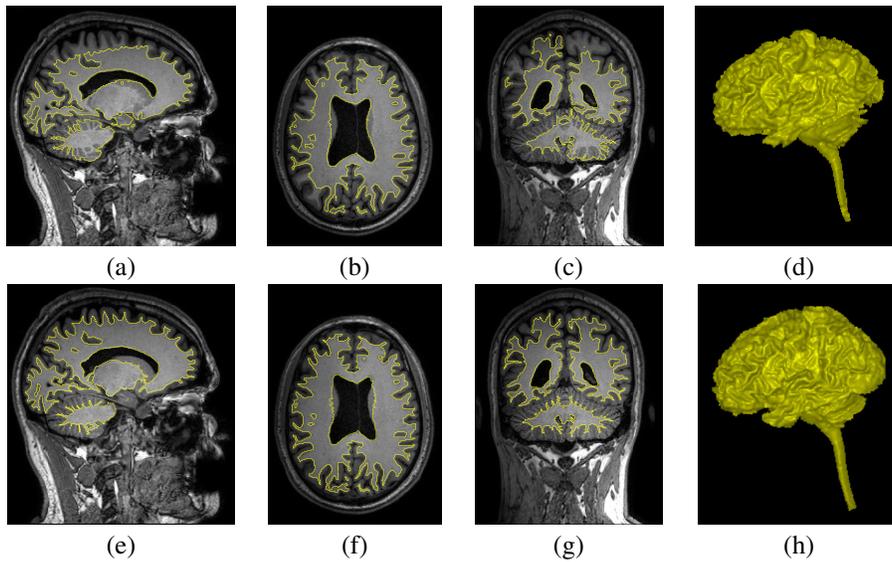
Fig. 8.   White matter segmentation in 3D for the same user-selected markers. Results by (a-d) f_{max} over an enhanced gradient, and (e-h) $f^{lex}_{\sum|\triangle I|}$.

V. Boundary Polarity via NSCF

Boundary-based segmentation methods such as like live wire [6], [10], can easily incorporate boundary orientation to resolve between very similar nearby boundary segments (Figure 9), by favoring segmentation on a single orientation (e.g., *counter-clockwise* orientation).
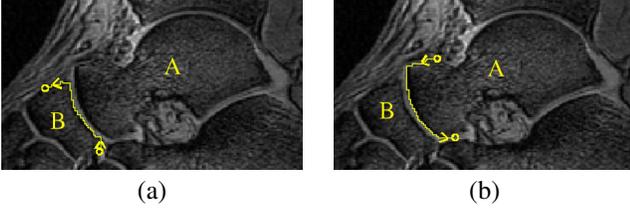
Fig. 9. Example of boundary-based segmentation, where the boundary-orientedness property of live wire helps it to distinguish between two similar boundary segments from the distinct objects A and B [38].

In [25], [26] we successfully incorporated the boundary polarity constraint in the IFT using NSCF in digraphs, resulting in a novel method called ***Oriented Image Foresting Transform*** (OIFT).

In the case of digraphs, there are two different types of cut for each object boundary: an inner-cut boundary composed by arcs that point toward object pixels $\mathcal{C}_i(L)$ (Figure 10a) and an outer-cut boundary with arcs from object to background pixels $\mathcal{C}_o(L)$ (Figure 10b).

$$\mathcal{C}_i(L) = \{(s,t) \in \boldsymbol{\xi} \mid L(s) = 0,\ L(t) = 1\} \quad (12)$$

$$\mathcal{C}_o(L) = \{(s,t) \in \boldsymbol{\xi} \mid L(s) = 1,\ L(t) = 0\} \quad (13)$$
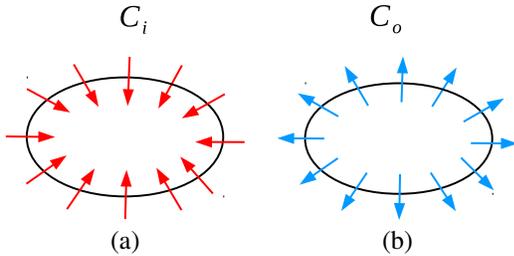
Fig. 10. Schematic representation of (a) inner cuts and (b) outer cuts.

Consequently, we consider two different types of energy, E_i (Equation 14) and E_o (Equation 15).

$$E_i(L,G) = \min_{(s,t)\ \in\ \mathcal{C}_i(L)} \omega(s,t) \quad (14)$$

$$E_o(L,G) = \min_{(s,t)\ \in\ \mathcal{C}_o(L)} \omega(s,t) \quad (15)$$

We use a digraph, where $\omega(s,t)$ is a combination of a regular undirected dissimilarity measure $\psi(s,t)$, multiplied by an orientation factor, as follows:

$$\omega(s,t) = \begin{cases} \psi(s,t) \times (1+\alpha) & \text{if } I(s) > I(t), \\ \psi(s,t) \times (1-\alpha) & \text{otherwise.} \end{cases} \quad (16)$$

Several different procedures can be adopted for $\psi(s,t)$, such as the absolute value of the difference of image intensities (i.e., $\psi(s,t) = |I(t) - I(s)|$). Note that we have $\omega(s,t) \neq \omega(t,s)$ when $\alpha > 0$.

The OIFT is build upon the IFT framework by considering one of the following path functions in a symmetric digraph:

$$f_{i,\max}^{bkg}(\langle t \rangle) = \begin{cases} -1 & \text{if } t \in \mathcal{S}_o \cup \mathcal{S}_b \\ +\infty & \text{otherwise} \end{cases}$$

$$f_{i,\max}^{bkg}(\pi_{r \rightsquigarrow s} \cdot \langle s,t \rangle) = \begin{cases} Expr1 & \text{if } r \in \mathcal{S}_o \\ Expr2 & \text{if } r \in \mathcal{S}_b \end{cases} \quad (17)$$

$$Expr1 = \max\{f_{i,\max}^{bkg}(\pi_{r \rightsquigarrow s}), 2 \times \omega(t,s) + 1\}$$

$$Expr2 = \max\{f_{i,\max}^{bkg}(\pi_{r \rightsquigarrow s}), 2 \times \omega(s,t)\}$$

$$f_{o,\max}^{bkg}(\langle t \rangle) = \begin{cases} -1 & \text{if } t \in \mathcal{S}_o \cup \mathcal{S}_b \\ +\infty & \text{otherwise} \end{cases}$$

$$f_{o,\max}^{bkg}(\pi_{r \rightsquigarrow s} \cdot \langle s,t \rangle) = \begin{cases} Expr1 & \text{if } r \in \mathcal{S}_o \\ Expr2 & \text{if } r \in \mathcal{S}_b \end{cases} \quad (18)$$

$$Expr1 = \max\{f_{o,\max}^{bkg}(\pi_{r \rightsquigarrow s}), 2 \times \omega(s,t) + 1\}$$

$$Expr2 = \max\{f_{o,\max}^{bkg}(\pi_{r \rightsquigarrow s}), 2 \times \omega(t,s)\}$$

$$f_{i,\omega}(\langle t \rangle) = \begin{cases} -1 & \text{if } t \in \mathcal{S}_o \cup \mathcal{S}_b \\ +\infty & \text{otherwise} \end{cases}$$

$$f_{i,\omega}(\pi_{r \rightsquigarrow s} \cdot \langle s,t \rangle) = \begin{cases} \omega(t,s) & \text{if } r \in \mathcal{S}_o \\ \omega(s,t) & \text{if } r \in \mathcal{S}_b \end{cases} \quad (19)$$

$$f_{o,\omega}(\langle t \rangle) = \begin{cases} -1 & \text{if } t \in \mathcal{S}_o \cup \mathcal{S}_b \\ +\infty & \text{otherwise} \end{cases}$$

$$f_{o,\omega}(\pi_{r \rightsquigarrow s} \cdot \langle s,t \rangle) = \begin{cases} \omega(s,t) & \text{if } r \in \mathcal{S}_o \\ \omega(t,s) & \text{if } r \in \mathcal{S}_b \end{cases} \quad (20)$$

Figure 11 shows an example demonstrating that the function $f_{o,\max}^{bkg}$ is not smooth.
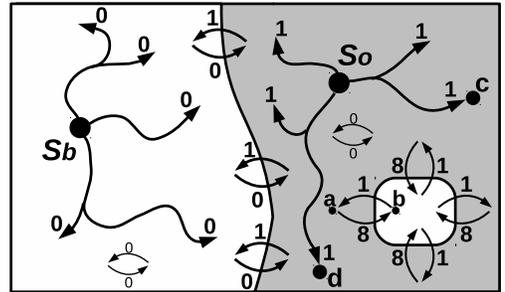
Fig. 11. The function $f_{o,\max}^{bkg}$ process reversed edges for paths from $\mathcal{S}_b$. Suppose that $\mathcal{S}_b$ conquers the left white region with 0 cost, since its arcs are interconnected by 0-weighted arcs. The pixels within the gray region have also 0-weighted arcs, so $\mathcal{S}_o$ provides better costs to them ($2 \times 0 + 1 = 1$ against $2 \times 1 = 2$ offered by $\mathcal{S}_b$). The best cost offered by $\mathcal{S}_o$ to the node b is $2 \times 8 + 1 = 17$, while $\mathcal{S}_b$ could have provided a better cost to b ($2 \times 1 = 2$), but b is assigned to the object. Thus, the function is not smooth.

The segmentation using $f_{i,\max}^{bkg}$ or $f_{i,\omega}$ favors transitions from dark to bright pixels, and $f_{o,\max}^{bkg}$ or $f_{o,\omega}$ favors the opposite orientation (Figure 12), according to Theorem 1. In the case of multiple candidate segmentations with the same energy, $f_{i,\omega}$ and $f_{o,\omega}$ produces a better handling of the *tie zones* than $f_{i,\max}^{bkg}$ and $f_{o,\max}^{bkg}$, respectively (Figure 13) [26].
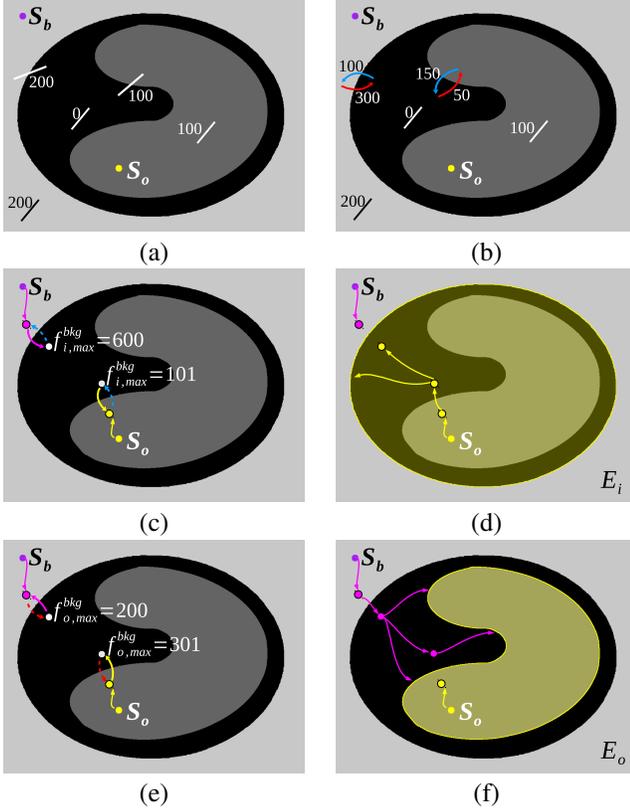
Fig. 12. (a) A synthetic image with internal and external seeds ($\mathcal{S}_o$ and $\mathcal{S}_b$). Some representative arc values $\omega(s,t)$ are depicted for each region and border segment. (b) Arc values $\omega(s,t)$ for border segments according to Equation 16 with $\alpha = 0.5$. (c-d) Transition from dark to bright pixels favors the segmentation using $f_{i,\max}^{bkg}$ and maximizes $E_i(L, G)$. (e-f) Transition from bright to dark pixels favors the segmentation using $f_{o,\max}^{bkg}$ and maximizes $E_o(L, G)$.

Theorem 1 (Inner/outer-cut boundary optimality). *For two given sets of seeds $\mathcal{S}_o$ and $\mathcal{S}_b$, any spanning forest computed by the IFT algorithm for function $f_{o,\max}^{bkg}$ or $f_{o,\omega}$ defines an optimum cut that maximizes $E_o(L, G)$ among all possible segmentation results satisfying the hard constraints. Any spanning forest computed by the IFT algorithm for function $f_{i,\max}^{bkg}$ or $f_{i,\omega}$ defines an optimum cut that maximizes $E_i(L, G)$ among all possible segmentation results satisfying the hard constraints.*

In our experiments, we used four 2D datasets, to segment different objects in MRI and CT slice images; two 3D datasets of MR images and one dataset of colored images. In the first experiment, we used 40 slice images from real MR images of the foot, and we computed the mean performance curve for the functions $f_{\max}^{bkg}$, $f_{o,\max}^{bkg}$ and $f_{i,\max}^{bkg}$, to segment the talus bone, for different seed sets obtained by eroding and dilating the ground truth, as shown in Figure 14a-b. For the second
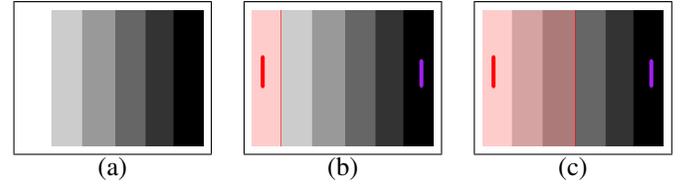
Fig. 13. (a) Input image with equally weighted transitions, having the same orientation. (b) The OIFT result using $f_{o,\max}^{bkg}$ as proposed in [25] assigns the ambiguous regions to the background. (c) OIFT using $f_{o,\omega}$ with a *FIFO* tie-breaking policy gives more equally balanced partitions.
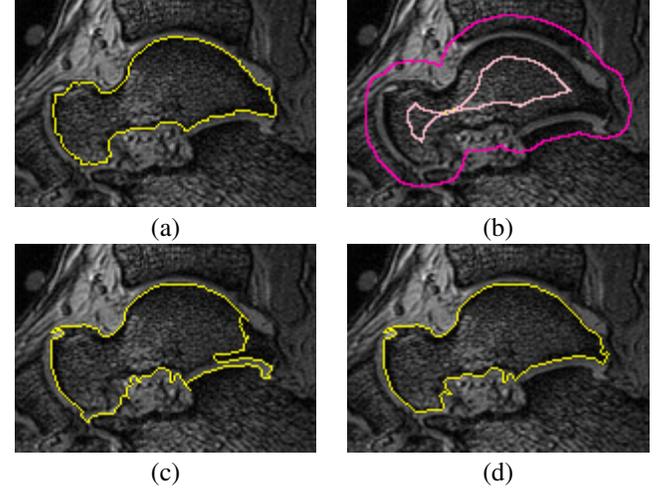
Fig. 14. (a) True segmentation of the talus in an MR image of a foot. (b) Seed sets obtained by eroding and dilating the true segmentation. (c) Segmentation result by IRFC. (d) An improved segmentation result is obtained by exploiting the boundary orientation using $f_{i,\max}^{bkg}$.

dataset, we performed the segmentation of the calcaneus for all the connectivity functions, using 40 slices from MR images of the foot. In the third experiment, 40 slice images were selected from CT cervical spine studies of 10 subjects to segment the spinal-vertebra. Finally, 40 slice images from CT thoracic studies of 10 subjects were used to segment the liver. This gave us a total of 160 2D-images to be processed by each function. The experimental accuracy curves are given in Figures 15, 16, 17 and 18, which show that whenever the object presents transitions from dark to bright pixels $f_{i,\max}^{bkg}$ gives the best accuracy results, and whenever there are transitions from bright to dark pixels $f_{o,\max}^{bkg}$ obtains the top accuracy. Note also that $f_{i,\max}^{bkg}$ gives the best results when $f_{o,\max}^{bkg}$ presents the worst accuracy, and vice versa. This means that by specifying the wrong orientation, it becomes even harder to get the desired boundary as compared to the undirected approach $f_{\max}^{bkg}$, as we expected.

In the 3D experiments, first we used a dataset of 3D MRI images, composed of brain images of 20 normal subjects. We performed the 3D segmentation of the cerebelum for the functions $f_{\max}^{bkg}$, $f_{i,\max}^{bkg}$ and $f_{o,\max}^{bkg}$ in all volumes. Figure 19 shows the obtained results, which indicate that $f_{o,\max}^{bkg}$ improves the accuracy.

Second, we used 20 real volumetric MR images of the foot in 3D. We computed the mean performance curve (Dice

Method	Description	Graph Type
$IRFC$	Iterative Relative Fuzzy Connectedness [16]	undirected graph
IFT_{FIFO}^{max}	Traditional IFT with f_{max} and FIFO tie-breaking policy, as described in [18]	undirected graph
$PW_{q=2}$	The power watershed algorithm [23]	undirected graph
$OIFT_{inner}^{max}$	OIFT result using $f_{i,max}^{bkg}$	weighted digraph
$OIFT_{outer}^{max}$	OIFT result using $f_{o,max}^{bkg}$	weighted digraph
$OIFT_{inner}^{\omega}$	OIFT using $f_{i,\omega}$	weighted digraph
$OIFT_{outer}^{\omega}$	OIFT using $f_{o,\omega}$	weighted digraph

TABLE I. DESCRIPTION OF THE METHODS USED IN THE EXPERIMENTS.
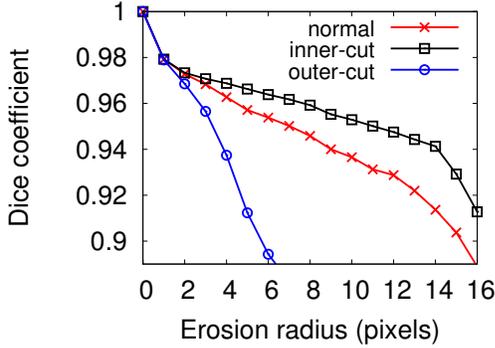
Fig. 15. The mean accuracy curves for f_{max}^{bkg} (normal), $f_{i,max}^{bkg}$ (inner), $f_{o,max}^{bkg}$ (outer) for the segmentation of talus.
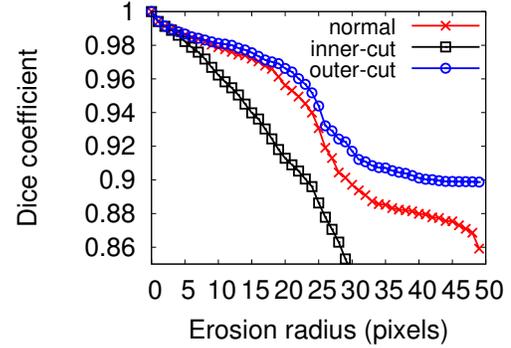
Fig. 18. The mean accuracy curves for f_{max}^{bkg} (normal), $f_{i,max}^{bkg}$ (inner), $f_{o,max}^{bkg}$ (outer) for the segmentation of liver.
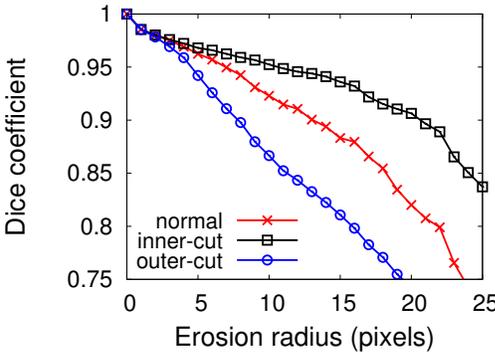
Fig. 16. The mean accuracy curves for f_{max}^{bkg} (normal), $f_{i,max}^{bkg}$ (inner), $f_{o,max}^{bkg}$ (outer) for the segmentation of calcaneus.
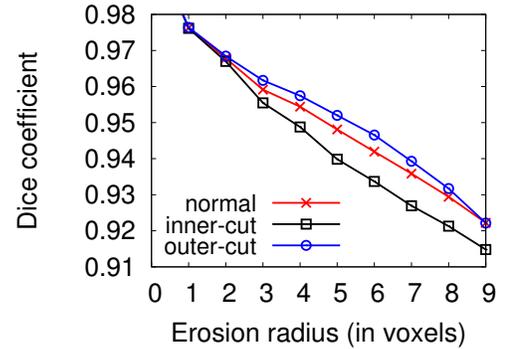
Fig. 19. Mean accuracy curves for f_{max}^{bkg} (normal), $f_{i,max}^{bkg}$ (inner), $f_{o,max}^{bkg}$ (outer) for the 3D segmentation of the cerebellum.
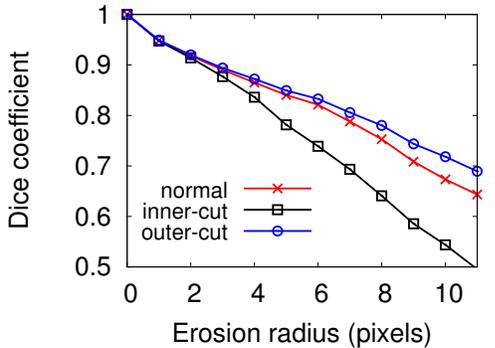
Fig. 17. The mean accuracy curves for f_{max}^{bkg} (normal), $f_{i,max}^{bkg}$ (inner), $f_{o,max}^{bkg}$ (outer) for the segmentation of spinal-vertebra.

coefficient) for all the methods depicted on Table I [26]. The experimental accuracy curves with the Sobel gradient (Figure 20) show that whenever the object presents transitions from dark to bright pixels, as it is the case with the bones talus and calcaneus, $f^{i,\omega}$ and $f_{i,max}^{bkg}$ give the best accuracy results. Note also that $f_{o,max}^{bkg}$ and $f_{o,\omega}$ present the worst accuracy values, by specifying the wrong orientation.

In the experiment with colored images, we used 50 natural images with known true segmentations obtained from [39]. The arc weights were computed by the method proposed in [24], using a few manual-selected training markers to estimate the color models. Figure 21 shows the experimental curves, where $f_{o,\omega}$ provided better mean results. Note that $f_{i,\omega}$ presented the worst accuracy values in this case, since it considers the wrong boundary orientation.
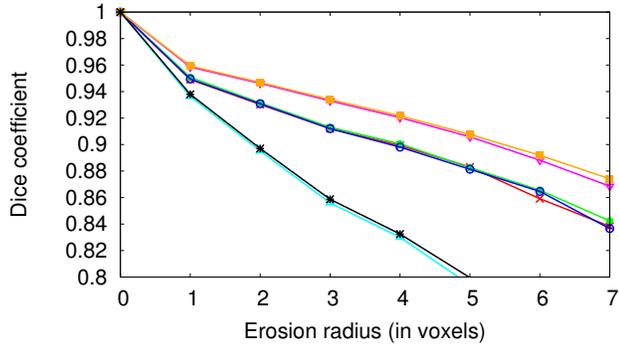
Fig. 20. The mean accuracy curves (Dice) using the Sobel gradient for the 3D segmentation of: (a) talus, and (b) calcaneus.
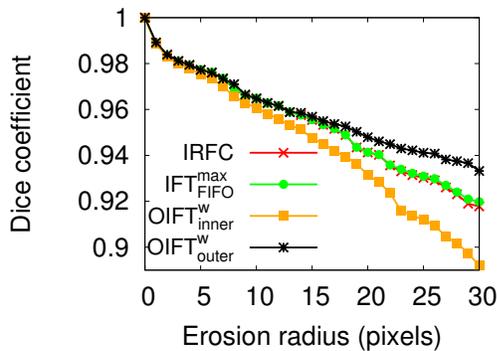
Fig. 21. The mean accuracy curve for different methods using color images.

Fig. 22. (a) MR image of the brain (object with regular shape). (b) Image gradient. (c) Segmentation result of the brain by IFT with $f_{\max}$, which outputs a very irregular shape.

VI. SHAPE CONSTRAINTS VIA NSCF

Structures poorly defined in medical images, as well as natural images, are often hard to be segmented due to their low contrast in relation to other nearby false boundaries (Figure 22). The usage of shape constraints can help to alleviate part of this problem for objects that have a more regular shape.

Shape constraints, such as the star-convexity prior introduced by Veksler [40], can limit the search space of possible delineations to a smaller subset, thus eliminating false candidate boundaries. In this context, a point p is said to be visible to c via a set $\mathcal{O}$ if the line segment joining p to c lies in the set $\mathcal{O}$. An object $\mathcal{O}$ is star-convex with respect to center c, if every point $p \in \mathcal{O}$ is visible to c via $\mathcal{O}$ (Figure 23). In the case of multiple stars, a computationally tractable definition, was proposed in [37], using a *Geodesic Star Convexity* (GSC) constraint in the segmentation by *min-cut/max-flow*.
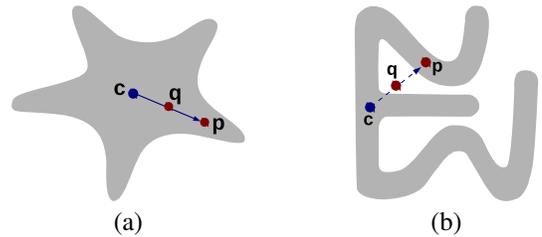
Fig. 23. For any point p within the object and the star center c, we have: (a) a star-convex object and (b) a non-star-convex object.

In [27], we proposed a new algorithm (Algorithm 1) that incorporates the GSC constraint in the energy maximization by IFT [31], favoring the segmentation of objects with more regular shape, resulting in a novel method called ***IFT with Geodesic Star Convexity Constraints*** (GSC–IFT). In this method, the set of star centers is taken as the set of internal seeds ($\mathcal{S}_o$), and the line segments are the paths that form a spanning forest rooted at the internal seeds. The arc weights $\omega_2(s, t)$ in the path-extension rule for f_{sum} (Equation 2) are given by:

$$\omega_2(s, t) = [\omega(s, t) + 1]^{\beta} - 1 + \|t - s\| \qquad (21)$$

where $\|t - s\|$ is the Euclidean distance between pixels s and t, and β controls the forest topology.

For lower values of β ($\beta \approx 0.0$), $\omega_2(s, t)$ approaches $\|t - s\|$, and the forest topology becomes similar to the Euclidean shortest-path forest (Figure 24a). For higher values, $[\omega(s, t) + 1]^{\beta}$ dominates the expression, and the greater the intensity-based dissimilarity, the greater is its influence over the results (Figure 24b-d).

Figure 25 shows how the parameter β affects the forest for f_{sum}, and its corresponding segmentation with shape constraints. Clearly, for lower values of β the method imposes more star regularization to the object's boundary, while for higher values of β, it allows a better fit to the curved protrusions and indentations of the boundary.
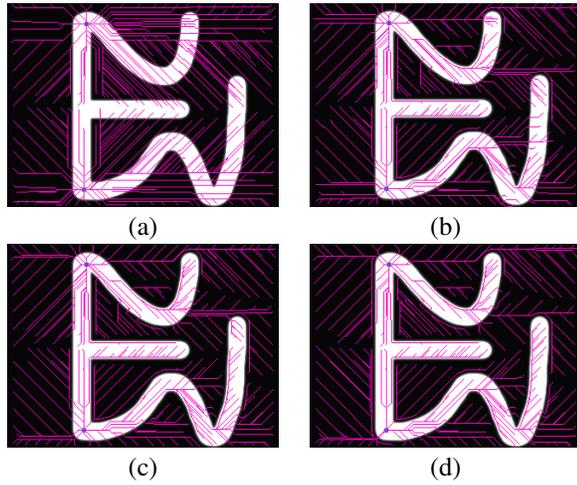
Fig. 24. The effects of the power parameter β over the forest topology: The optimum-path forest of f_{sum} for: (a) $\beta = 0.0$, (b) $\beta = 0.3$, (c) $\beta = 0.4$, and (d) $\beta = 0.5$.
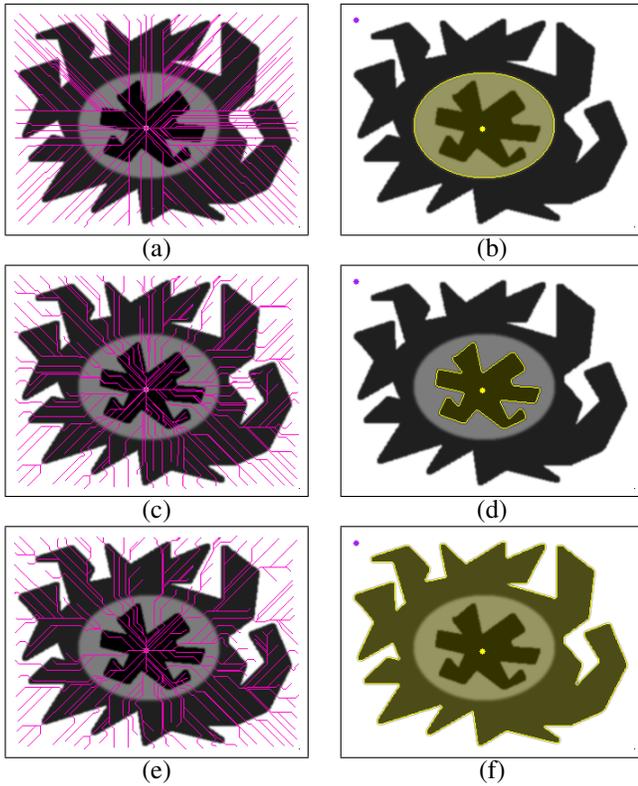
Fig. 25. The effects of the power parameter β over the forest topology: (a) The optimum-path forest of f_{sum} for $\beta = 0$, and (b) its resulting segmentation by the GSC–IFT algorithm (Algorithm 1). Similar results for: (c-d) $\beta = 0.3$, and (e-f) $\beta = 0.5$.

Algorithm 1 obtains a segmentation that maximizes a graph-cut measure among all possible segmentation results satisfying the shape constraints by *Geodesic Star Convexity* (GSC), whose theoretical proof of its optimality has been proved in [27]. In its first step (Line 1), the optimum forest P_{sum} for f_{sum} (Equation 2) is computed by invoking the regular IFT algorithm, using only $\mathcal{S}_o$ (set of star centers) as seeds. The subsequent Lines 2–8 are similar to the original

IFT with f_ω (Equation 3). The differences arise from this point (Lines 9–12).

Algorithm 1. – GSC-IFT ALGORITHM

INPUT: Graph $G = \langle \mathcal{I}, \boldsymbol{\xi}, \omega \rangle$, and seed sets $\mathcal{S}_o$ and $\mathcal{S}_b$.
OUTPUT: Minimum path-value map V, and label map L.
AUXILIARY: Optimum-path forest P_{sum}, priority queue Q, variable tmp, and an array of $status$.

1.   *Compute $P_{sum} \leftarrow IFT(G, \mathcal{S}_o, \emptyset, f_{sum})$.*
2.   **For each** $t \in \mathcal{S}_o$, **do** $L(t) \leftarrow 1$.
3.   **For each** $t \in \mathcal{S}_b$, **do** $L(t) \leftarrow 0$.
4.   **For each** $t \in \mathcal{I}$, **do**
5. $Set\ V(t) \leftarrow f_\omega(\langle t \rangle)$, *and set* $status(t) \leftarrow 0$.
6.   **If** $V(t) \neq +\infty$, **then** *insert t in Q.*
7.   **While** $Q \neq \emptyset$, **do**
8.   *Remove s from Q such that $V(s)$ is minimum.*
9.   **If** $L(s) = 1$, **then**
10. $Conquer\_Path(s, G, P_{sum}, V, Q, L, status)$.
11.   **Else If** $L(s) = 0$, **then**
12. $Prune\_Tree(s, G, P_{sum}, V, Q, L, status)$.

Algorithm 2. – CONQUER_PATH ALGORITHM

INPUT: Image pixel $s \in \mathcal{I}$, image graph $G = \langle \mathcal{I}, \boldsymbol{\xi}, \omega \rangle$, optimum-path forest P_{sum}, value map V, priority queue Q, label map L, and an array of $status$.

1. $x \leftarrow s$.
2.   **do**
3.   **If** $x \in Q$, **then** *Remove x from Q*
4.   *Set* $status(x) \leftarrow 1$, $L(x) \leftarrow 1$.
5.   **For each** $y \in \boldsymbol{\xi}(x)$, *such that* $status(y) \neq 1$, **do**
6.   *Compute* $tmp \leftarrow f_\omega(\pi_x \cdot \langle x, y \rangle)$.
7.   **If** $tmp < V(y)$ *and* $y \neq Psum(x)$, **then**
8.   **If** $y \in Q$, **then** *remove y from Q.*
9.   *Set* $V(y) \leftarrow tmp$, $L(y) \leftarrow 1$.
10.   *Insert y in Q.*
11.   *Set* $x \leftarrow Psum(x)$.
12.   **While** $(x \neq nil$ *and* $status(x) \neq 1)$

Algorithm 3. – PRUNE_TREE ALGORITHM

INPUT: The same parameters as in Algorithm 2.
AUXILIARY: FIFO queue Q_{FIFO}, variable tmp, and x.

1. $x \leftarrow s$.
2.   **If** $x \in Q$, **then** *Remove x from Q*
3.   *Set* $status(x) \leftarrow 1$, $L(x) \leftarrow 0$, *and insert x in Q_{FIFO}.*
4.   **While** $Q_{FIFO} \neq \emptyset$
5.   *Remove x from Q_{FIFO}* .
6.   **For each** $y \in \boldsymbol{\xi}(x)$, *such that* $status(y) \neq 1$, **do**
7.   **If** $Psum(y) = x$, **then**
8.   *insert y in Q_{FIFO}*
9.   **If** $y \in Q$, **then** *remove y from Q*
10.   *Set* $status(y) \leftarrow 1$, $L(y) \leftarrow 0$
11.   **Else**
12.   *Compute* $tmp \leftarrow f_\omega(\pi_x \cdot \langle x, y \rangle)$.
13.   **If** $tmp < V(y)$, **then**
14.   **If** $y \in Q$, **then** *remove y from Q.*
15.   *Set* $V(y) \leftarrow tmp$, $L(y) \leftarrow 0$.
16.   *Insert y in Q.*

Figure 26 shows an example of image segmentation using the GSC–IFT algorithm (Algorithm 1).
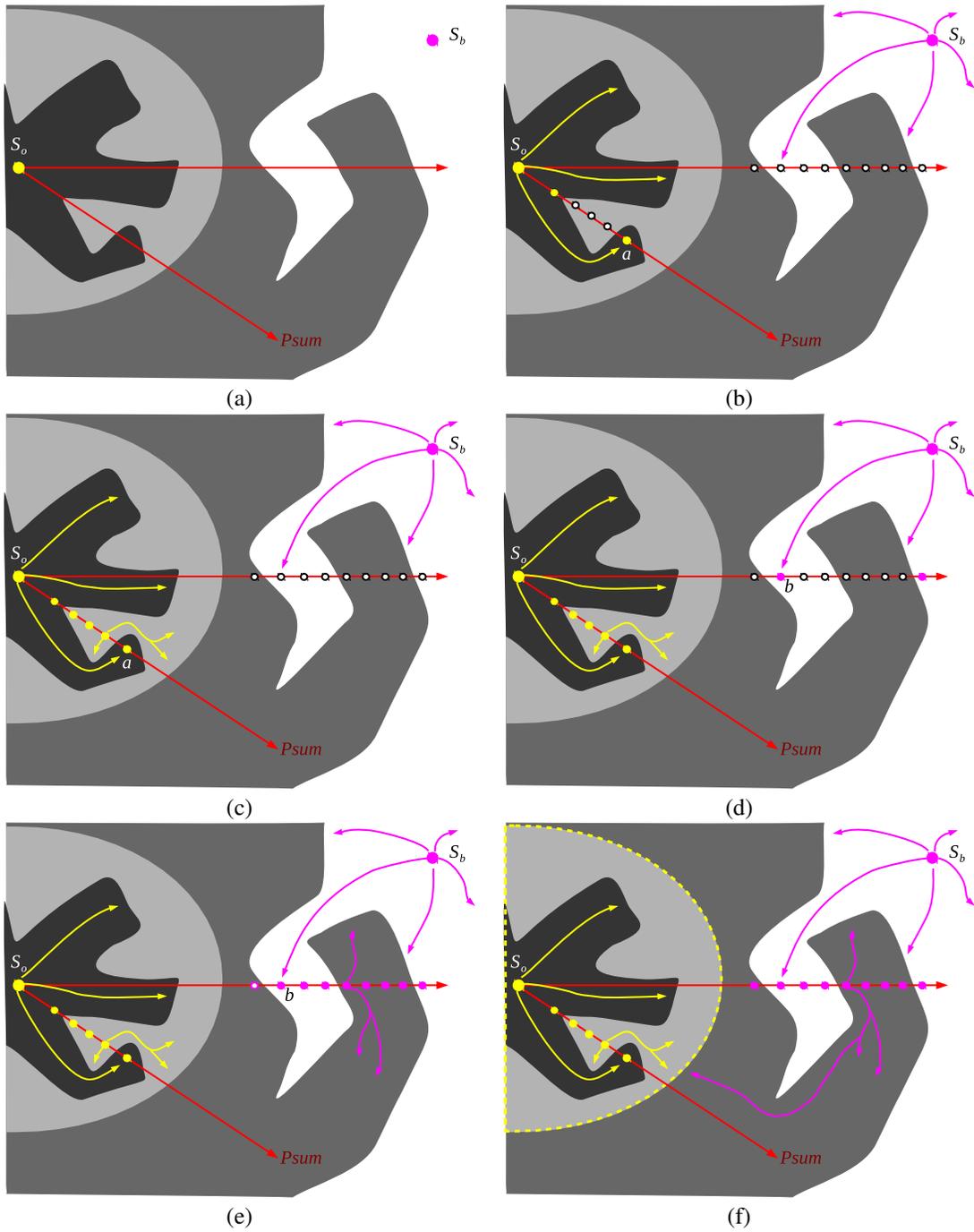
Fig. 26. (a) Synthetic image with three possible boundary cuts, where s_o e s_b are seeds of the object and background, respectively; and the forest P_{sum} permits the visibility of the shape constraints. The target object has a regular shape. (b) After the pixel a leaves of the queue Q with label 1, we have the violation of visibility of the pixel a respect to its closest seed s_o. (c) The subroutine *ConquerPath* (Algorithm 2) assigns label 1 to all his predecessors, allowing the expansion of the object paths in light gray region. (d) The pixel b leaves of the queue Q with label of the background, blocking the visibility of their descendants in P_{sum} respect to s_o. (e) The subroutine *PruneTree* (Algorithm 3) assigns label 0 to their descendants, allowing the expansion of the background paths in the dark gray region. (f) Segmentation result (dashed yellow line) with the GSC–IFT algorithm corresponds with the characteristic of the target object.

In Figures 27 and 28 we present examples of the talus and breast segmentation, respectively. Figure 29 shows an example of 3D segmentation from user-selected markers in MR-T1 images, where the graph's nodes are the voxels, and the arcs are defined between 6-neighbors. Figure 30 shows some results for colored images, with the arc weights computed as in [24]. It is quite clear the advantages of considering the GSC–IFT method.

(a)   (b)
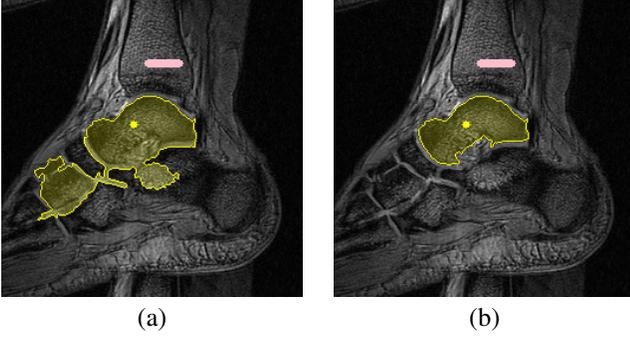
Fig. 27. Segmentation of the talus in a MR image of a foot for the selected markers: (a) IRFC. (b) An improved result by GSC-IFT ($\beta = 0.5$).

(a)   (b)

(c)   (d)
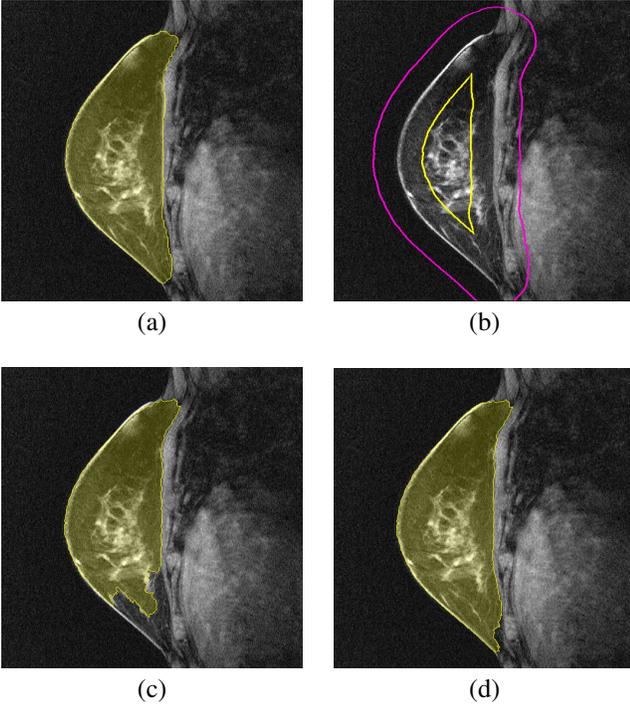
Fig. 28. (a) True segmentation of the breast in MRI. (b) Example of seed sets obtained by eroding and dilating the true segmentation. (c) Segmentation result by IRFC. (d) An improved result is obtained by exploiting the Geodesic Star Convexity (GSC-IFT).

Later, in [28] we proposed the novel method called ***OIFT with Geodesic Star Convexity*** (GSC–OIFT), which incorporate Gulshan's geodesic star convexity prior in the OIFT approach for interactive image segmentation, in order to simultaneously handle boundary polarity and shape constraints (Theorem 2). This method permits the customization of the segmentation by IFT to better match the features of a particular target object (Figure 31). We constrain the search for optimum result, that

(a)   (b)

(c)   (d)
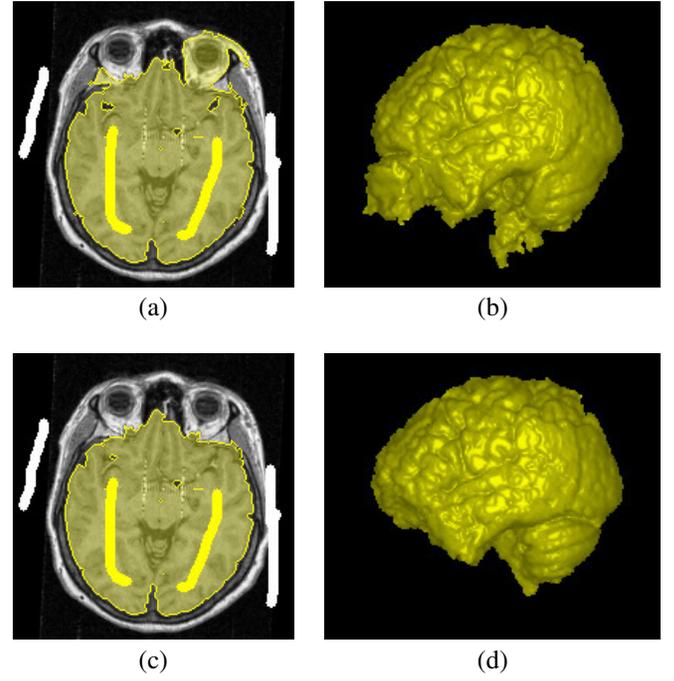
Fig. 29. Example of 3D skull stripping from user-selected markers. (a-b) Segmentation result by IFT with $f_{\max}$. (c-d) An improved result is obtained by exploiting the Geodesic Star Convexity (GSC–IFT with $\beta = 0.1$).

maximize the graph-cut measures E_i (Equation 14) or E_o (Equation 15), only to segmentations that satisfy the geodesic star convexity constraint. We compute a geodesic forest P_{sum} for f_{sum} (Equation 2) by the regular IFT algorithm, using only $\boldsymbol{\mathcal{S}_o}$ as seeds, for the given digraph G, obtaining two sets of arcs $\boldsymbol{\xi^i_{P_{sum}}}$ (Equation 22) and $\boldsymbol{\xi^o_{P_{sum}}}$ (Equation 23). The GSC constraint is violated when $\boldsymbol{\mathcal{C}_i}(L) \cap \boldsymbol{\xi^i_{P_{sum}}} \neq \emptyset$ or $\boldsymbol{\mathcal{C}_o}(L) \cap \boldsymbol{\xi^o_{P_{sum}}} \neq \emptyset$ (Figure 32).

Theorem 2 (Inner/outer-cut boundary optimality). *For a given image graph $G = \langle \boldsymbol{\mathcal{V}}, \boldsymbol{\xi}, \omega \rangle$, consider a modified weighted graph $G' = \langle \boldsymbol{\mathcal{V}}, \boldsymbol{\xi}, \omega' \rangle$, with weights $\omega'(s,t) = -\infty$ for all $(s,t) \in \boldsymbol{\xi^o_{P_{sum}}}$, and $\omega'(s,t) = \omega(s,t)$ otherwise. For two given sets of seeds $\boldsymbol{\mathcal{S}_o}$ and $\boldsymbol{\mathcal{S}_b}$, the segmentation computed over G' by the IFT algorithm for function $f^{bkg}_{o,\max}$ defines an optimum cut in the original graph G, that maximizes $E_o(L, G)$ among all possible segmentation results satisfying the shape constraints by the geodesic star convexity, and the seed constraints. Similarly, the segmentation computed by the IFT algorithm for function $f^{bkg}_{i,\max}$, over a modified graph $G' = \langle \boldsymbol{\mathcal{V}}, \boldsymbol{\xi}, \omega' \rangle$; with weights $\omega'(s,t) = -\infty$ for all $(s,t) \in \boldsymbol{\xi^i_{P_{sum}}}$, and $\omega'(s,t) = \omega(s,t)$ otherwise; defines an optimum cut in the original graph G, that maximizes $E_i(L, G)$ among all possible segmentation results satisfying the shape constraints by the geodesic star convexity.*

$$\boldsymbol{\xi^i_{P_{sum}}} = \{(s,t) \in \boldsymbol{\xi} \mid s = P_{sum}(t)\} \qquad (22)$$

$$\boldsymbol{\xi^o_{P_{sum}}} = \{(s,t) \in \boldsymbol{\xi} \mid t = P_{sum}(s)\} \qquad (23)$$

Figure 33 shows an example of the GSC–OIFT method with the non-smooth function $f^{bkg}_{o,\max}$.
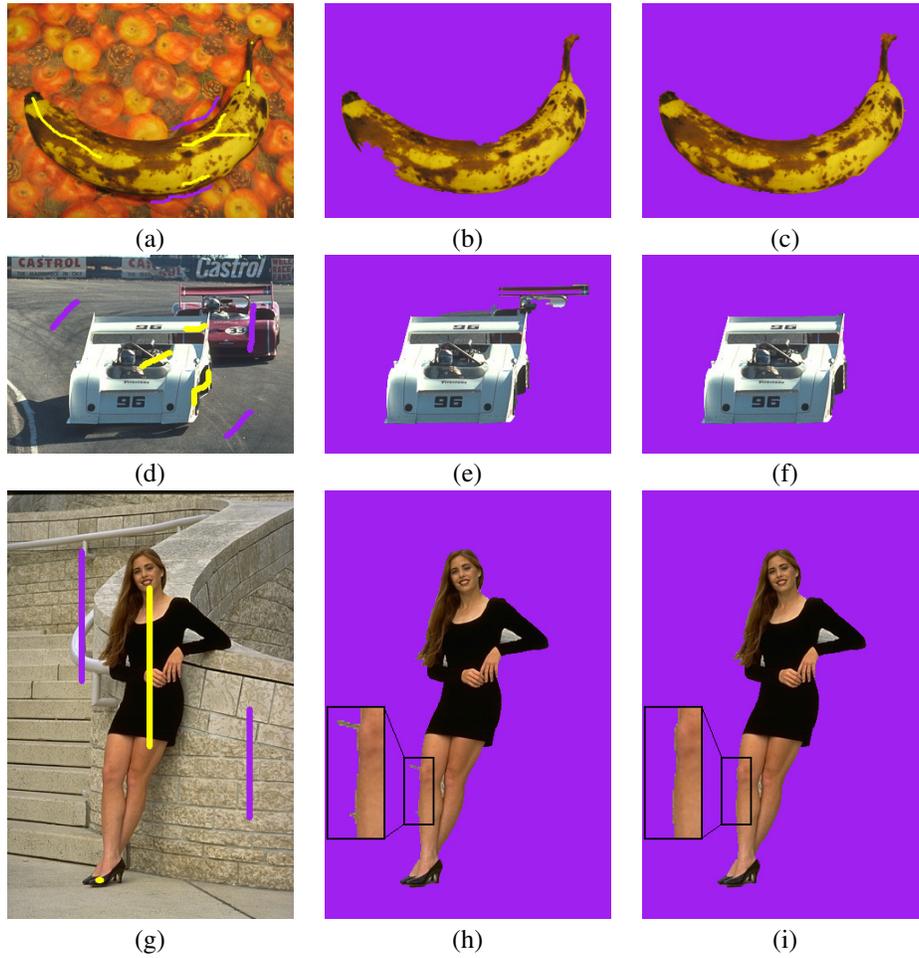
Fig. 30. (a,d,e) Input image with user-selected markers. (b,e,f) Segmentation result by IFT with $f_{\max}$. (c,f,i) Segmentation result by GSC–IFT ($\beta = 0.1$).
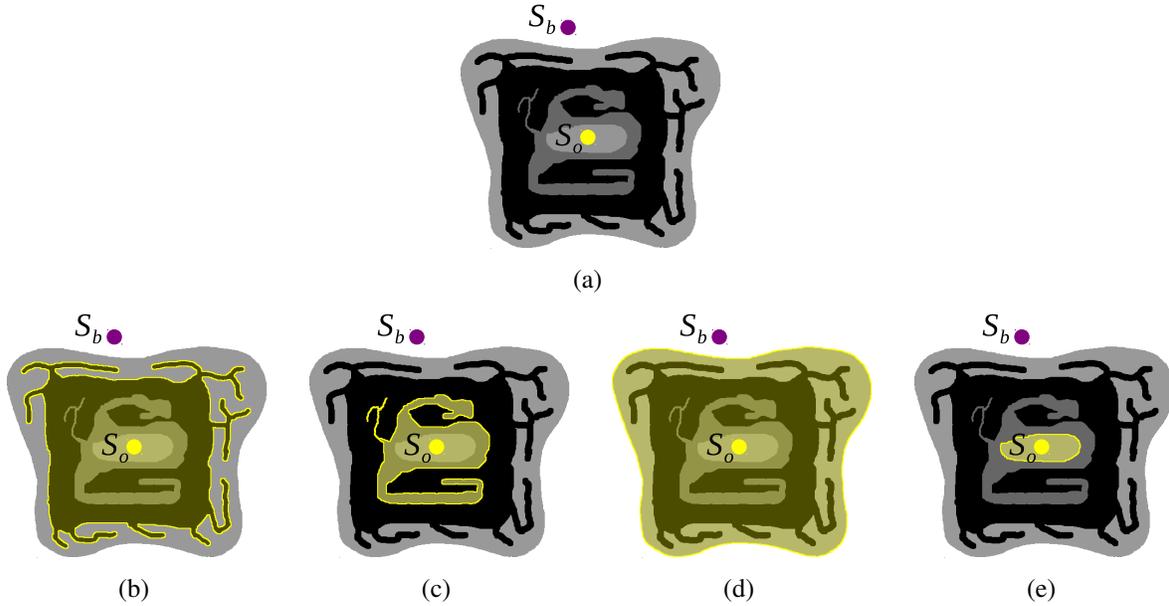
Fig. 31. (a) Synthetic image with selected markers $\mathcal{S}_o$ and $\mathcal{S}_b$. The target object has a regular shape with transitions from bright to dark in its border. Segmentation results by: (b) IFT obtains a non-regular shape and wrong orientation, (c) $OIFT_{outer}^{\max}$ obtains a non-regular shape, (d) GSC–IFT obtains a wrong orientation and (e) GSC–$OIFT_{outer}^{\max}$ (simultaneously considering boundary polarity and shape constraints) obtains a correct matching with the characteristics of the target object.
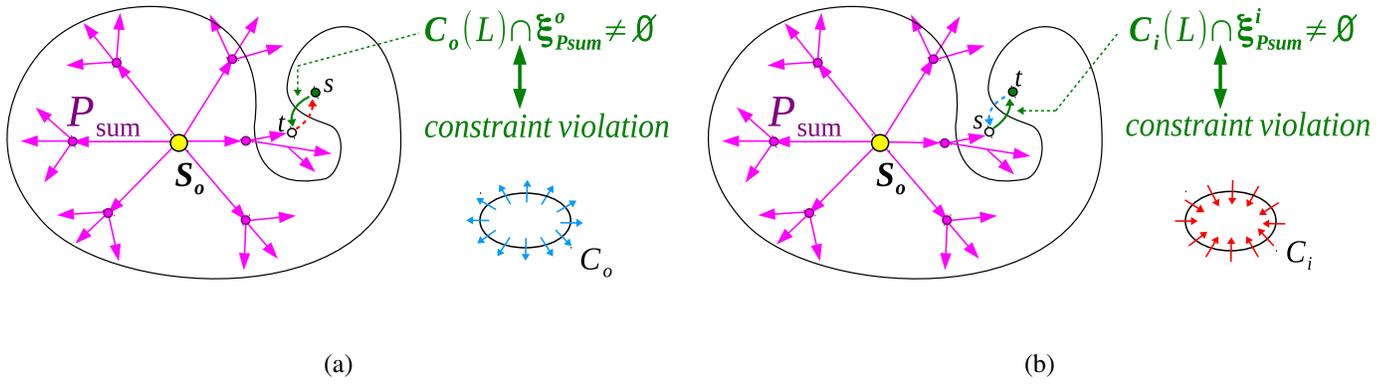
Fig. 32. The GSC constraint is violated when: (a) there is an arc $(s, t) \in \mathcal{C}_{i}(L) \cap \boldsymbol{\xi}^{i}_{P_{sum}}$, or (b) there is an arc $(s, t) \in \mathcal{C}_{o}(L) \cap \boldsymbol{\xi}^{o}_{P_{sum}}$.
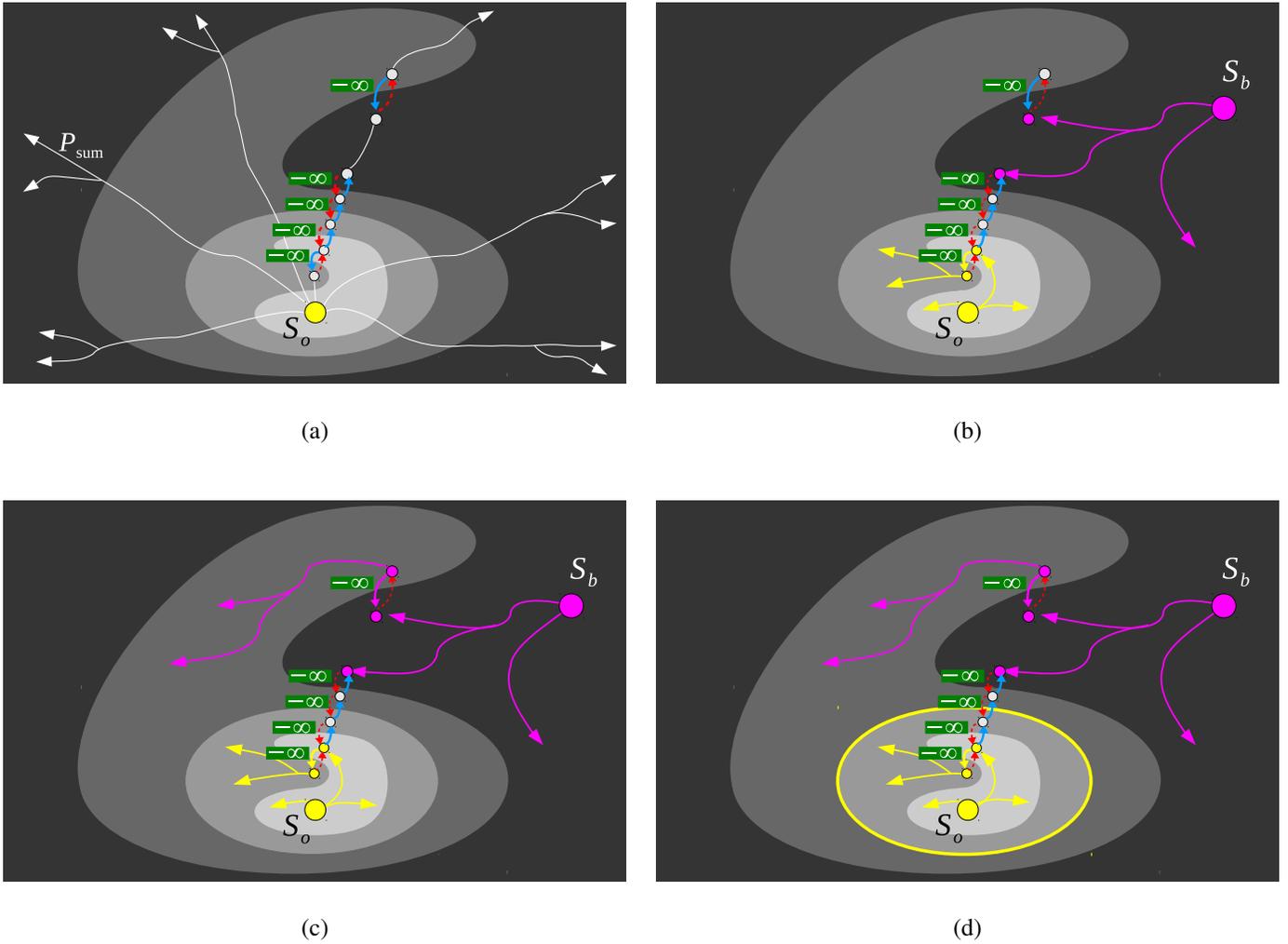
Fig. 33. (a) Synthetic image with three possible boundary cuts with same orientation (bright to dark), forest P_{sum} and internal seed s_o (star center). The arcs with value $-\infty$ represent arcs $(s, t) \in \boldsymbol{\xi}^{o}_{P_{sum}}$, which violate the shape constraints by the GSC. The blue arrows represent outer cuts in the boundaries and the red (dotted arrows) inner cuts. (b) Pixels are conquered by the internal seed s_o. (c) Pixels are conquered by the external seed s_b. (d) Segmentation result (yellow line) by GSC–OIFT with $f^{bkg}_{o,\max}$.

In our experiments, we used 40 image slices of 10 thoracic CT studies to segment the liver. Figure 34a shows the mean accuracy curves for all the images assuming different seed sets obtained by eroding and dilating the ground truth. Note that for higher values of β, GSC–OIFT imposes less shape constraints, so that the accuracy tends to decrease (Figures 34b-d). Figure 35 shows some results in the case of user-selected markers for the liver, and Figure 36 shows one example in 3D.
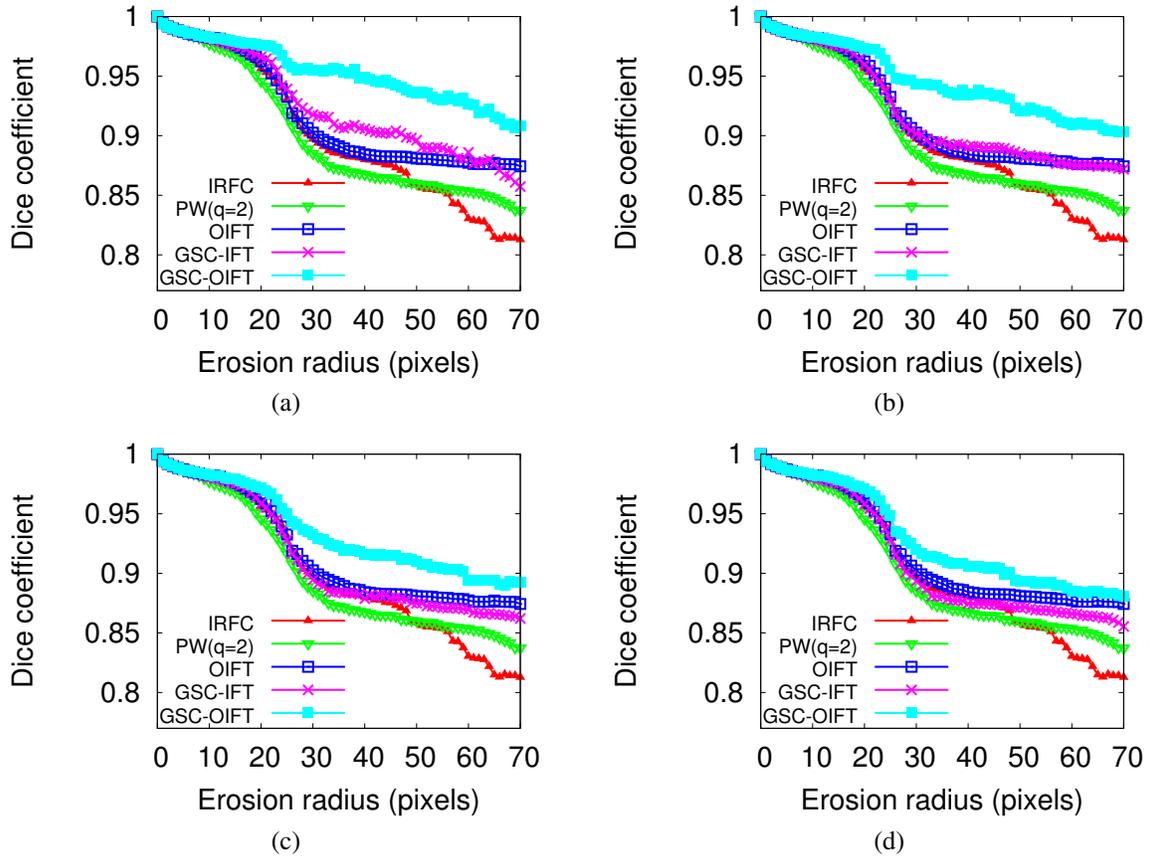
Fig. 34. The mean accuracy curves of all methods for the liver segmentation for various values of β: (a) $\beta = 0.0$, (b) $\beta = 0.2$, (c) $\beta = 0.5$, and (d) $\beta = 0.7$.
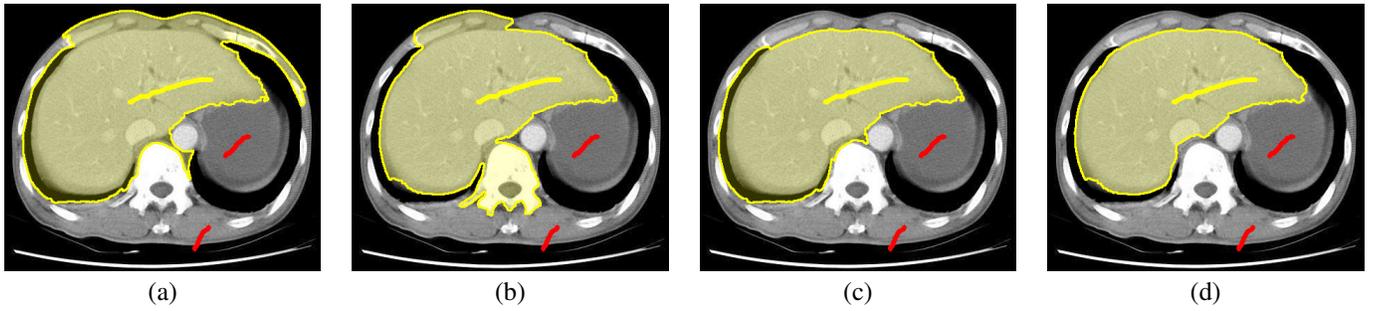
Fig. 35. Results for user-selected markers: (a) IRFC, (b) OIFT ($f_{o,\max}^{bkg}$ with $\alpha = 0.5$), (c) GSC–IFT ($\beta = 0.7$), and (d) GSC–OIFT ($\beta = 0.7$, $\alpha = 0.5$).
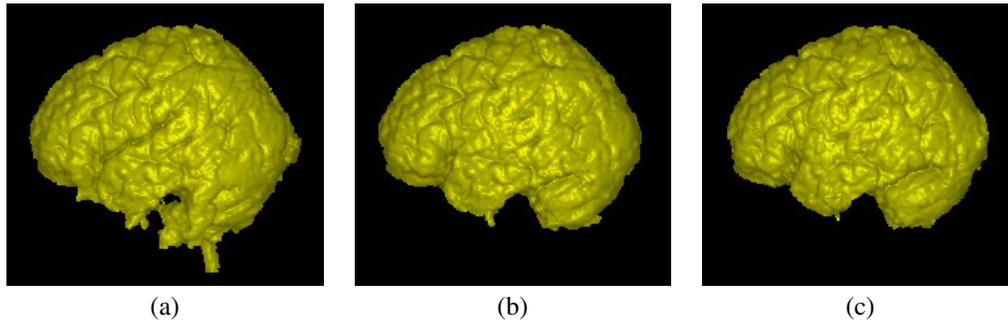
Fig. 36. Example of 3D skull stripping in MRI: (a) IRFC (IFT with $f_{\max}$), (b) GSC-IFT ($\beta = 0.3$, $\alpha = 0.0$), and (c) GSC-OIFT ($\beta = 0.3$, $\alpha = 0.5$), for the same user-selected markers.

VII. Conclusion

The proposed extension GSC–OIFT includes the IFT with $f_{\max}$, OIFT and GSC–IFT as particular cases, depending on the configuration of its parameters α and β. Note that the adaptive functions presented in Section IV can't be reduced to a GSC–OIFT computation. Table II presents an useful classification of the proposed methods in the master's dissertation [30], according to the specific image characteristics.

The theoretical foundation proposed in this work has also allowed new achievements that were recently published, such as [41] and [42]. The project also contributed in a FINEP project (1266/13) in biomedical engineering, CNPq project (486083/2013-6), and FAPESP project (2012/06911-2).

As future work, we intend to combine the proposed methods with statistical models to automatically define seeds for automatic segmentation.

References

[1] M. Sonka, R. Boyle, and V. Hlavac, *Image Processing, Analysis and Machine Vision*. ITP, 1999.

[2] P. Suetens, *Fundamentals of Medical Imaging*. Cambridge University Press, 2009.

[3] A. Madabhushi and J. Udupa, "Interplay between intensity standardization and inhomogeneity correction in mr image processing," *IEEE TMI*, vol. 24, no. 5, pp. 561–576, 2005.

[4] X. Bai and G. Sapiro, "Distance cut: interactive segmentation and matting of images and videos," in *IEEE International Conference on Image Processing (ICIP)*, vol. 2, San Antonio, Texas, 2007, pp. II – 249–II – 252.

[5] J. Wang and M. Cohen, "An iterative optimization approach for unified image segmentation and matting," in *ICCV '05: Proceedings of the Tenth IEEE International Conference on Computer Vision*. Washington, DC, USA: IEEE Computer Society, 2005, pp. 936–943.

[6] A. Falcão, J. Udupa, S. Samarasekera, S. Sharma, B. Hirsch, and R. Lotufo, "User-steered image segmentation paradigms: Live-wire and live-lane," *Graphical Models and Image Processing*, vol. 60, no. 4, pp. 233–260, Jul 1998.

[7] Y. Boykov and G. Funka-Lea, "Graph cuts and efficient N-D image segmentation," *International Journal of Computer Vision*, vol. 70, no. 2, pp. 109–131, 2006.

[8] M. Kass, A. Witkin, and D. Terzopoulos, "Snakes: Active contour models," *International Journal of Computer Vision*, vol. 1, no. 4, pp. 321–331, 1987.

[9] J. Cousty, G. Bertrand, L. Najman, and M. Couprie, "Watershed cuts: Thinnings, shortest path forests, and topological watersheds," *IEEE Transactions on Pattern Analysis and Machine Intelligence*, vol. 32, pp. 925–939, 2010.

[10] E. Mortensen and W. Barrett, "Interactive segmentation with intelligent scissors," *Graphical Models and Image Processing*, vol. 60, pp. 349–384, 1998.

[11] P. Saha and J. Udupa, "Relative fuzzy connectedness among multiple objects: theory, algorithms, and applications in image segmentation," *Computer Vision and Image Understanding*, vol. 82, no. 1, pp. 42–56, 2001.

[12] W.Yang, J.Cai, J. Zheng, and J. Luo, "User-friendly interactive image segmentation through unified combinatorial user inputs," *IEEE Transactions on Image Processing*, vol. 19, no. 9, pp. 2470–2479, Sep 2010.

[13] L. Vincent and P. Soille, "Watersheds in digital spaces: An efficient algorithm based on immersion simulations," *IEEE Transactions on Pattern Analysis and Machine Intelligence*, vol. 13, no. 6, Jun 1991.

[14] J. Roerdink and A. Meijster, "The watershed transform: Definitions, algorithms and parallelization strategies," *Fundamenta Informaticae*, vol. 41, pp. 187–228, 2000.

[15] L. Grady, "Random walks for image segmentation," *IEEE Transactions on Pattern Analysis and Machine Intelligence*, vol. 28, no. 11, pp. 1768–1783, 2006.

[16] K. Ciesielski, J. Udupa, P. Saha, and Y. Zhuge, "Iterative relative fuzzy connectedness for multiple objects with multiple seeds," *Computer Vision and Image Understanding*, vol. 107, no. 3, pp. 160–182, 2007.

[17] Y. Boykov and M. Jolly, "Interactive graph cuts for optimal boundary & region segmentation of objects in N-D images," in *International Conference on Computer Vision (ICCV)*, vol. 1, 2001, pp. 105–112.

[18] A. Falcão, J. Stolfi, and R. Lotufo, "The image foresting transform: Theory, algorithms, and applications," *IEEE Transactions on Pattern Analysis and Machine Intelligence*, vol. 26, no. 1, pp. 19–29, 2004.

[19] V. Vezhnevets and V. Konouchine, ""growcut" - interactive multi-label N-D image segmentation by cellular automata," in *Proc. Graphicon.*, 2005, pp. 150–156.

[20] A. Sinop and L. Grady, "A seeded image segmentation framework unifying graph cuts and random walker which yields a new algorithm," in *11th International Conference on Computer Vision (ICCV)*. IEEE Computer Society, 2007.

[21] P. Miranda and A. Falcão, "Elucidating the relations among seeded image segmentation methods and their possible extensions," in *XXIV Conference on Graphics, Patterns and Images (SIBGRAPI)*. Maceió, AL: Los Alamitos: IEEE Computer Society, Aug 2011.

[22] K. Ciesielski, J. Udupa, A. Falcão, and P. Miranda, "A unifying graph-cut image segmentation framework: algorithms it encompasses and equivalences among them," in *Proceedings of SPIE on Medical Imaging*, vol. 8314, San Diego, California, USA, 2012.

[23] C. Couprie, L. Grady, L. Najman, and H. Talbot, "Power watersheds: A unifying graph-based optimization framework," *Transactions on Pattern Analysis and Machine Intelligence*, vol. 99, 2010.

[24] P. Miranda, A. Falcão, and J. Udupa, "Synergistic arc-weight estimation for interactive image segmentation using graphs," *Computer Vision and Image Understanding*, vol. 114, no. 1, pp. 85–99, 2010.

[25] P. Miranda and L. Mansilla, "Oriented image foresting transform segmentation by seed competition," *IEEE Transactions on Image Processing*, vol. 23, no. 1, pp. 389–398, Jan 2014.

[26] L. Mansilla and P. Miranda, "Image segmentation by oriented image foresting transform: Handling ties and colored images," in *18th International Conference on Digital Signal Processing (DSP)*. Santorini, Greece: IEEE, Jul 2013, pp. 1–6.

[27] L. Mansilla, M. Jackowski, and P. Miranda, "Image foresting transform with geodesic star convexity for interactive image segmentation," in *IEEE International Conference on Image Processing (ICIP)*, Melbourne, Australia, Sep 2013, pp. 4054–4058.

[28] L. Mansilla and P. Miranda, "Image segmentation by oriented image foresting transform with geodesic star convexity," in *Computer Analysis of Images and Patterns (CAIP)*, vol. 8047, York, UK, Aug 2013, pp. 572–579.

[29] L. Mansilla, F. Cappabianco, and P. Miranda, "Image segmentation by image foresting transform with non-smooth connectivity functions," in *XXVI Conference on Graphics, Patterns and Images (SIBGRAPI)*. Arequipa, Perú: IEEE, Aug 2013, pp. 147–154.

[30] L. Mansilla, "Image foresting transform with non-smooth connectivity functions: Adaptive weights, boundary polarity, and shape constraints," Master's thesis, Institute of Mathematics and Statistics, University of São Paulo, Brazil, Feb 2014. [Online]. Available: http://www.teses.usp.br/teses/disponiveis/45/45134/tde-17032014-121734/pt-br.php

[31] P. Miranda and A. Falcão, "Links between image segmentation based on optimum-path forest and minimum cut in graph," *Journal of Math-*

Image characteristics	Proposed method
Presence of inhomogeneity effects.	IFT with $f_{\Sigma\|\triangle\mathcal{I}\|}^{lex}$ or $f_{\updownarrow}^{lex}$.
Transitions of pixels in the object boundary from dark to bright without shape constraint.	OIFT with $f_{i,\max}^{bkg}$ ($\alpha >= 0.5$), OIFT with $f_{i,\omega}$ ($\alpha >= 0.5$) or GSC–OIFT with $f_{i,\omega}$ ($\beta >= 1.0$ and $\alpha >= 0.5$).
Transitions of pixels in the object boundary from bright to dark without shape constraint.	OIFT with $f_{o,\max}^{bkg}$ ($\alpha >= 0.5$), OIFT with $f_{o,\omega}$ ($\alpha >= 0.5$) or GSC–OIFT with $f_{o,\omega}$ ($\beta >= 1.0$ and $\alpha >= 0.5$).
Object with strict regular shape (star convex) and transition of pixels in its boundary from dark to bright.	GSC–OIFT with $f_{i,\max}^{bkg}$ ($\beta = 0$ and $\alpha >= 0.5$).
Object with strict regular shape (star convex) and transition of pixels in its boundary from bright to dark.	GSC–OIFT with $f_{o,\max}^{bkg}$ ($\beta = 0$ and $\alpha >= 0.5$).
Object with regular shape (star convex) allowing a certain degree of variability in its shape, and transition of pixels in its boundary from dark to bright.	GSC–OIFT with $f_{i,\max}^{bkg}$ ($\beta > 0$ and $\alpha >= 0.5$).
Object with regular shape (star convex) allowing a certain degree of variability in its shape, and transition of pixels in its boundary from bright to dark.	GSC–OIFT with $f_{o,\max}^{bkg}$ ($\beta > 0$ and $\alpha >= 0.5$).

TABLE II.   RELATION OF THE PROPOSED METHODS AND THE IMAGE TYPE TO SEGMENT.

ematical Imaging and Vision, vol. 35, no. 2, pp. 128–142, 2009, doi: 10.1007/s10851-009-0159-9.

[32] K. Ciesielski, J. Udupa, A. Falcão, and P. Miranda, "Comparison of fuzzy connectedness and graph cut segmentation algorithms," in *Proceedings of SPIE on Medical Imaging: Image Processing*, vol. 7962, Orlando, 2011.

[33] P. Miranda, A. Falcão, and T. Spina, "Riverbed: A novel user-steered image segmentation method based on optimum boundary tracking," *IEEE Transactions on Image Processing*, vol. 21, no. 6, pp. 3042–3052, 2012, doi:10.1109/TIP.2012.2188034.

[34] A. Falcão, F. Bergo, F. Favretto, G. Ruppert, P. Miranda, and F. Cappabianco, *Neurociências e epilepsia. Capítulo: Processamento, Visualização e Análise de Imagens Anatômicas do Cérebro Humano*. Plêiade, 2008, vol. 1, série CInAPCe.

[35] P. Miranda, A. Falcão, and J. Udupa, "Cloud bank: A multiple clouds model and its use in MR brain image segmentation," in *Proceedings of the IEEE International Symposium on Biomedical Imaging (ISBI)*, Boston, MA, 2009, pp. 506–509.

[36] F. Cappabianco, P. Miranda, J. Ide, C. Yasuda, and A. Falcão, "Unraveling the compromise between skull stripping and inhomogeneity correction in 3T MR images," in *Conference on Graphics, Patterns and Images (SIBGRAPI 2012)*, Aug 2012, pp. 1–8.

[37] V. Gulshan, C. Rother, A. Criminisi, A. Blake, and A. Zisserman, "Geodesic star convexity for interactive image segmentation," in *Proceedings of Computer Vision and Pattern Recognition*, 2010, pp. 3129–3136.

[38] A. Falcão, J. Udupa, and F. Miyazawa, "An ultra-fast user-steered image segmentation paradigm: Live-wire-on-the-fly," *IEEE Transactions on Medical Imaging*, vol. 19, no. 1, pp. 55–62, Jan 2000.

[39] C. Rother, V. Kolmogorov, A. Blake, and M. Brown, "Image and video editing: Grabcut," http://research.microsoft.com/en-us/um/cambridge/projects/visionimagevideoediting/segmentation/grabcut.htm.

[40] O. Veksler, "Star shape prior for graph-cut image segmentation," in *European Conference on Computer Vision (ECCV)*, vol. 5304, 2008, pp. 454–467.

[41] C. Braz and P. Miranda, "Image segmentation by image foresting transform with geodesic band constraints," in *IEEE International Conference on Image Processing (ICIP)*, Paris, France, Oct 2014, pp. 4333 – 4337.

[42] H. Bejar and P. Miranda, "Oriented relative fuzzy connectedness: Theory, algorithms, and applications in image segmentation," in *XXVII Conference on Graphics, Patterns and Images (SIBGRAPI)*. Rio de Janeiro, Brazil: IEEE, Aug 2014, pp. 304–311.